

1 Deforestation as an anthropogenic driver of
2 mercury pollution

3 *Aryeh Feinberg^{a*}, Martin Jiskra^{b*}, Pasquale Borrelli^c, Jagannath Biswakarma^{b,d}, and*
4 *Noelle E. Selin^{a,e}*

5 ^a Institute for Data, Systems, and Society, Massachusetts Institute of Technology,
6 Cambridge, MA 02139, USA

7 ^b Environmental Geosciences, University of Basel, Basel 4056, Switzerland

8 ^c Department of Science, Roma Tre University, Rome 00146, Italy

9 ^d Department of Water Resources and Drinking Water, Eawag, Dübendorf 8600,
10 Switzerland

11 ^e Department of Earth, Atmospheric, and Planetary Sciences, Massachusetts Institute of
12 Technology, Cambridge, MA 02139, USA

13 *Correspondence to: arifeinberg@gmail.com (A.F.); martin.jiskra@gmail.com (M.J.)

14

15 KEYWORDS. Mercury (Hg), land use change, emissions, Minamata Convention,
16 Amazon rainforest, reforestation, chemical-transport modeling.

17

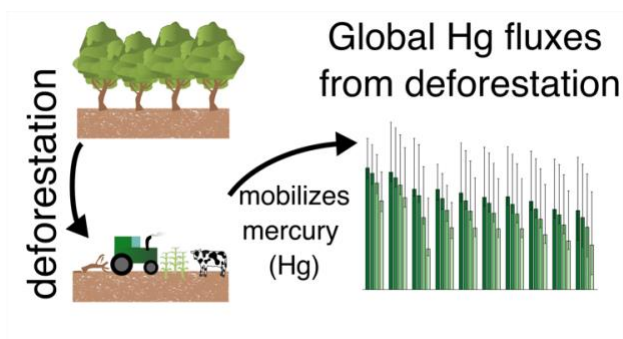
18 **Abstract**

19 Deforestation reduces the capacity of the terrestrial biosphere to take up the toxic
20 pollutant mercury (Hg) and enhances the release of secondary Hg from soils. The
21 consequences of deforestation for Hg cycling are not currently considered by
22 anthropogenic emissions inventories or specifically addressed under the global Minamata
23 Convention on Mercury. Using global Hg modeling constrained by field observations, we
24 estimate that net Hg fluxes to the atmosphere due to deforestation are 217 Mg yr^{-1} (95%
25 confidence interval, CI: $134\text{--}1650 \text{ Mg yr}^{-1}$) for 2015, approximately 10% of global
26 primary anthropogenic emissions. If deforestation of the Amazon rainforest continues at
27 business-as-usual rates, net Hg emissions from the region will increase by 153 Mg yr^{-1} by
28 2050 (CI: $97\text{--}418 \text{ Mg yr}^{-1}$), enhancing the transport and subsequent deposition of Hg to
29 aquatic ecosystems. Substantial Hg emissions reductions are found for two potential
30 cases of land use policies: conservation of the Amazon rainforest (92 Mg yr^{-1} , CI: 59 to
31 234 Mg yr^{-1}) and global reforestation (98 Mg yr^{-1} , CI: 64 to 449 Mg yr^{-1}). We conclude
32 that deforestation-related emissions should be incorporated as an anthropogenic source in
33 Hg inventories, and that land use policy could be leveraged to address global Hg
34 pollution.

35 **Synopsis**

36 This study quantifies the impact of deforestation on the global Hg cycle, finding that
37 deforestation increases Hg fluxes to air and water. Conservation and reforestation are
38 important policy tools to mitigate these fluxes.

39 **TOC Graphic**



40

41 *Main Text*

42 **Introduction**

43 Humans are exposed to the organic form of mercury (Hg), methylmercury (MeHg),
44 mainly through seafood consumption¹. Methylmercury is a potent neurotoxin, impairing
45 the neurodevelopment of fetuses and children and costing the global economy \$20–117
46 billion annually according to some estimates^{2,3}. Mercury is emitted to the atmosphere by:
47 a) primary anthropogenic sources, including artisanal and small-scale gold mining
48 (ASGM), fossil fuel combustion, and metal smelting; b) re-emissions of historical
49 anthropogenic (“legacy”) Hg from ocean and land; and c) geogenic sources⁴. Mercury
50 spreads globally in the atmosphere due to its overall elemental lifetime against deposition
51 of 4–6 months⁵. A global treaty, the Minamata Convention on Mercury, aims to protect
52 human health and the environment from anthropogenic emissions and releases of Hg. The
53 Convention targets primary anthropogenic emissions sources by phasing out Hg use and
54 adopting best available technologies for pollution control⁶. Primary anthropogenic
55 emissions account for only 30% of present-day total emissions, with legacy re-emissions
56 from land and ocean accounting for 60%⁷. The future of Hg pollution will depend not
57 only on reducing direct emissions through the Minamata Convention, but also on indirect
58 anthropogenic influences on legacy Hg emissions and fate.

59 Terrestrial ecosystems, and especially forests, are important sinks of Hg from the
60 atmosphere, taking up an estimated 2200–3600 Mg Hg per year⁸, more than a third of
61 total (anthropogenic, legacy, and geogenic) Hg emissions (7400 Mg yr⁻¹)⁹. By taking up
62 Hg, terrestrial ecosystems reduce the burden of Hg depositing in oceans and freshwater
63 systems, where it can be more readily converted to MeHg and bioaccumulated in fish.
64 Previous studies have drawn useful analogies between Hg and carbon cycling in
65 terrestrial ecosystems^{10,11}. Like carbon dioxide (CO₂), elemental mercury (Hg⁰) is
66 assimilated by foliage throughout the growing season¹². Mercury is transported from the
67 canopy to soil by foliage falling to the ground (“litterfall”) and dry deposited Hg being
68 washed off by precipitation (“throughfall”), which together are the major source (60–
69 90%) of Hg in soils⁸. Anthropogenic land use and land cover changes (LULCC),

70 including deforestation, perturb both CO₂ and Hg fluxes to the atmosphere^{13–15}. In the
71 case of carbon, scientific assessments¹⁴ have calculated the contribution of LULCC to
72 total anthropogenic CO₂ emissions (13% of total), and land management practices are
73 governed by Article 5 of the Paris Agreement¹⁶. For Hg, on the other hand, quantitative
74 estimates of the overall importance of land cover change are limited. Only one previous
75 study modeled the impact of future LULCC on atmospheric Hg cycling, focusing on the
76 effects of climate-induced changes to vegetation¹⁵. No anthropogenic Hg emissions
77 inventories have quantified the impacts of historical and future deforestation, and land
78 management is not currently addressed by Hg policy efforts like the Minamata
79 Convention.

80 Several processes mobilize Hg from terrestrial systems after deforestation. Along with
81 removing a strong atmospheric sink of Hg⁸, deforestation leads to more insolation
82 reaching the soil, which increases volatilization of Hg from soils through enhanced
83 microbial¹⁷ or photochemical¹⁸ reduction. Fire-mediated deforestation leads to direct
84 emission of Hg from forest and soil biomass¹⁹. Soils in deforested areas are subject to
85 accelerated erosion rates, enhancing Hg export to downstream ecosystems^{17,20,21}. Direct
86 measurement of deforestation-driven fluxes at larger scales is challenging given
87 variations in the land sink due to trends in environmental conditions, necessitating the use
88 of models to quantify these fluxes²². Models of terrestrial–atmosphere Hg fluxes, while
89 still much more uncertain than analogous carbon cycle models, are improving due to a
90 better process understanding and increasing availability of terrestrial
91 measurements^{8,12,23,24}. Thus, the time is ripe for assessing the relative importance of
92 deforestation-driven fluxes in the Hg cycle.

93 Policies on local, national, and international scales will shape the future evolution of
94 deforestation Hg fluxes. Deforestation due to agricultural land conversion threatens the
95 Amazon rainforest^{25,26}, which currently contributes 29% of the global land sink for
96 atmospheric Hg⁰ (ref. ²³). At current deforestation rates, 40% of the Amazon rainforest
97 could be lost by 2050, while enhanced environmental legislation (e.g., expansion of
98 protected areas and enforcement) can reduce the deforested area to 15% (ref. ²⁷).

99 Reforestation and afforestation on the global scale are being studied as part of the
100 solution to reach net zero greenhouse gas emissions in the future²⁸, though the efficacy of
101 these measures has been debated²⁹. In any case, the climate mitigation benefits of
102 forestation would not be realized without accompanying aggressive CO₂ emissions
103 reductions^{29,30}. Similarly, forest conservation and reforestation policies may have
104 potential benefits for Hg sequestration on land, yet the magnitude of impacts remain
105 unquantified.

106 Here, we apply the GEOS-Chem Hg model²³ to calculate deforestation emission factors
107 for Hg for different regions and evaluate them against available observations. We
108 quantify the global atmospheric Hg fluxes in 2015 that result from deforestation. We
109 study the impact of future Amazon deforestation policy scenarios²⁷ and potential global
110 reforestation efforts³⁰ on the terrestrial Hg sink, to investigate the importance of land
111 management policies for curbing Hg pollution.

112 **Materials and Methods**

113 *Atmospheric Hg model (GEOS-Chem) description.* In this study, we used the chemical-
114 transport model GEOS-Chem v12.8.1 with Hg⁰ dry deposition updates from Feinberg et
115 al.²³. The global model was run at 2.0° × 2.5° horizontal resolution and 47 vertical layers
116 up to 80 km altitude. The model tracks emissions, transport, chemistry, and deposition of
117 Hg in three chemical tracers: elemental mercury (Hg⁰), oxidized mercury (Hg^{II}), and
118 particulate-bound mercury (Hg^P). Atmospheric transport of Hg species is based on
119 MERRA-2 reanalysis meteorological data³¹. The Hg chemical mechanism assumes that
120 Br is the primary Hg⁰ oxidant and uses offline monthly maps of previously-calculated
121 oxidant concentrations to drive chemistry³². The aqueous photoreduction rate of Hg^{II} to
122 Hg⁰ is parametrized as a function of the organic aerosol concentration and the NO₂
123 photolysis rate³².

124 The wet removal of oxidized Hg (Hg^{II} and Hg^P) from the atmosphere is calculated in
125 online parametrizations considering large-scale and convective scavenging of gas and
126 particulate species³³. Dry deposition in GEOS-Chem applies a resistance-based
127 approach³⁴, which determines the dry deposition velocities depending on meteorology

128 (e.g., temperature and windspeed), land surface parameters (e.g., land type and leaf area
 129 index, LAI), and compound-specific parameters (biological reactivity, f_0 , and solubility,
 130 H^*). For Hg^0 , f_0 was set to 0.2 within the Amazon rainforest and 3×10^{-5} elsewhere.
 131 These values of f_0 were found to yield the best agreement with available measurements of
 132 Hg^0 vegetation uptake²³, though we later tested the impacts of uncertainties in these
 133 parameters on the modeling results (Section S4). The solubility of Hg^0 is low ($H^* = 0.11$
 134 M atm^{-1}), whereas gaseous Hg^{II} is assumed to be highly soluble ($H^* = 10^{14} \text{M atm}^{-1}$) and
 135 biologically unreactive ($f_0 = 0$). Dry deposition of Hg^{P} is determined according to the
 136 aerosol deposition parametrization in GEOS-Chem³⁵. Dry deposition is calculated
 137 separately over each land type within a grid cell (e.g., rainforest, grassland, cropland,
 138 etc.) and then an overall area-weighted average is calculated for the grid cell. GEOS-
 139 Chem accounts for 73 land types based on the Gibbs³⁶ land cover product. The LAI data
 140 for this study was taken from a reprocessed version of the Moderate Resolution Imaging
 141 Spectroradiometer (MODIS) satellite product³⁷.

142 Anthropogenic Hg emissions followed AMAP/UNEP estimates³⁸ for 2015. Biomass
 143 burning emissions were taken from the Global Fire Emissions Database (GFED) v4.1s³⁹.
 144 Fixed concentrations of Hg^0 in the surface ocean based on the MITgcm 3-D ocean
 145 model³² were used to calculate the Hg^0 air-sea exchange⁴⁰. We adopted a new
 146 formulation⁴¹ for the soil Hg^0 emissions parametrization (Supplementary Information,
 147 Section S1):

$$148 \quad E_{\text{soil}} = aC^b R_g^c \quad (\text{Eq. 1})$$

149 where E_{soil} is the Hg^0 emissions from soil (units $\text{ng m}^{-2} \text{h}^{-1}$), C is the concentration of Hg
 150 in soils (units $\mu\text{g g}^{-1}$), R_g is solar radiation flux at the ground (units W m^{-2}), and a , b , and
 151 c , are coefficients (set to 71, 2.5, and 0.76, respectively). The coefficients of this
 152 parametrization were tuned to match available soil emissions measurements (Section S1).
 153 The soil concentration map of Hg (C) was calculated using the method of Selin et al.⁴²,
 154 deriving the spatial distribution of soil concentrations by first assuming a steady state
 155 balance between land emissions and deposition in the preindustrial and subsequently
 156 increasing soil concentrations according to the distribution of anthropogenic Hg

157 deposition. As in Selin et al.⁴², the solar radiation at ground (R_g) is determined by
158 considering attenuation of the solar radiation flux (R_S) by shading from the overhead
159 canopy, parametrized by the LAI:

$$160 \quad R_g = R_S \exp\left(-\frac{\alpha \text{LAI}}{\cos\theta}\right) \quad (\text{Eq. 2})$$

161 where $\alpha = 0.5$, assuming extinction from a random angular distribution of leaves⁴³, and θ
162 is the solar zenith angle. Deforestation reduces the leaf area index (LAI) in impacted grid
163 cells, increasing the solar radiation flux at the ground (Eq. 2) and consequently enhancing
164 Hg^0 emissions from soils (Eq. 1). We have also updated GEOS-Chem to calculate soil
165 emissions at the sub-grid scale for each land use category contained within the grid cell.

166 **Reference (HIST) simulation.** We ran a GEOS-Chem simulation for the land cover and
167 LAI conditions of the year 2003 (HIST simulation), the first year where reprocessed LAI
168 data is available. To highlight the role of land cover changes alone, meteorological
169 conditions were kept constant by running all simulations with meteorology for 2014–
170 2015. We considered the first year as spinup to equilibrate the new land cover conditions,
171 and analyzed simulation differences for the meteorological year 2015.

172 **Estimating historical global deforestation-driven Hg emissions.** We calculated regional
173 emissions factors (EFs) for deforestation through conducting perturbation experiments in
174 GEOS-Chem. Emission factors were distinguished for the following regions based on
175 biogeographic realms⁴⁴: Palearctic, Nearctic, Afrotropic, Neotropic, Australasia &
176 Oceania, Indomalaya, China, and the Amazon rainforest (mapped in Fig. S5). We
177 separated China into its own region as soil Hg concentrations are higher than surrounding
178 areas due to historical Hg emissions. The Amazon rainforest was separated from other
179 Neotropic forests due to it having higher observed vegetation uptake fluxes and a
180 different assigned f_0 parameter in the model dry deposition scheme. For each region, a
181 simulation was conducted with perturbed land cover in the grid cells that experienced
182 deforestation during 2000–2014 in the $0.25^\circ \times 0.25^\circ$ resolution CMIP6 Land-Use
183 Harmonization (LUH2) dataset⁴⁵. As deforestation is mainly driven by agricultural
184 expansion^{46,47}, we replaced forest land cover in these grid cells with the most common

185 agricultural land cover relevant to the region: “Crops and Town” (Afrotropic,
 186 Indomalaya, Palearctic, Australasia & Oceania, and China), “Corns and Beans
 187 Croplands” (Neotropic and Nearctic), and “Fields and Woody Savannah” (Amazon). For
 188 the new agricultural areas, the LAI was set to the average annual cycle for the existing
 189 agricultural grid cells within the region. Eight deforestation (DFR) simulations (1 for
 190 each region) were conducted for 2014–2015, comparing year 2015 fluxes to the HIST
 191 simulation. To calculate the net emissions factor (EF) from deforestation, we calculated
 192 changes to the land-air exchange over the deforested grid cells:

$$193 \quad EF = \frac{(E_{DFR} - D_{DFR}) - (E_{HIST} - D_{HIST})}{A_{DFR}} \quad (\text{Eq. 3})$$

194 where E refers to Hg emissions, D refers to Hg deposition, and A refers to the area that is
 195 deforested in the simulation. The emissions factor represents the net emissions of Hg
 196 released by a deforested area annually, in units $\text{Mg m}^{-2} \text{yr}^{-1}$, capturing both the impact of
 197 increased soil Hg^0 emissions and reduced forest Hg^0 uptake. The assumption of linearity
 198 of the net emissions to deforested area holds in simulations conducted in the Amazon
 199 with differing spatial distributions of deforestation (Fig. S4), supporting an emissions
 200 factor approach to deforestation. We compared calculated emissions factors with existing
 201 estimates from observational studies^{18,21,24,48–64} for total deforestation EFs and the
 202 component of EFs due to soil Hg^0 emissions (Supplementary Information, Section S2).
 203 Based on our literature review (SI Spreadsheet), observational data is available for three
 204 of the tested regions (Amazon, China, and Nearctic).

205 We applied the regional emissions factor to historical land use data from the LUH2
 206 dataset to calculate emissions from deforestation. We defined gross deforested areas from
 207 the LUH2 dataset by summing the areas with transitions from primary or secondary
 208 forest to a non-forest land type. This approach does not consider LULCC fluxes due to
 209 harvesting of a forest without complete deforestation or the regrowth of vegetation after
 210 clearing, due to a lack of corresponding observations for Hg to constrain these
 211 parameters. Likewise, the emissions factors were assumed to be constant annually, so a
 212 deforested area continues to have the same total emissions for each year over the

213 considered time horizon. In reality, deforested areas could have a recovery timescale as
214 vegetation regrows, which is accounted for in carbon LULCC fluxes⁶⁵; for Hg, the
215 response timescales during regrowth are largely unknown. To account for these
216 uncertainties, we produced global and country-level estimates of Hg emissions in 2015
217 due to deforestation by summing deforestation over different time horizons: 15 years
218 (2000–2014), 30 years (1985–2014), 45 years (1970–2014), and 60 years (1955–2014).
219 The 45-year (1970–2014) accumulated results are presented in the main text, with the
220 others presented in Fig. S6.

221 ***Future Amazon deforestation scenarios.*** We employed deforestation scenarios from
222 Soares-Filho et al.²⁷, who developed a model for predicting the extent of deforestation
223 within the Amazon based on environmental policies and highway construction. They
224 presented two scenarios for 2050, encompassing a range of future deforestation
225 trajectories. In the Business as Usual (BAU) scenario, recent deforestation trends
226 continue into the future, assuming that compliance with conservation laws remains low
227 and no new areas will be protected. On the other hand, the Governance (GOV) scenario
228 assumes that the expansion of environmental legislation and increased enforcement of
229 protected areas will lead to a reduction in the deforestation rate. Compared to the
230 Amazon forest area in 2003 (5.3 million km²), in 2050 the BAU scenario projects 3.2
231 million km² remaining and GOV projects 4.5 million km² remaining²⁷. We focused our
232 analysis on comparing the forest coverage in the years 2003 and 2050.

233 We translated these scenarios into required inputs for the calculations in GEOS-Chem
234 (spatially gridded land use categories, LAI, and biomass burning emissions). The Soares-
235 Filho et al.²⁷ dataset assigns 1 km² pixels within the Amazon basin as being forested,
236 deforested, or agricultural areas for every year between 2003 and 2050. These annual
237 datasets were regridded to 0.25° × 0.25° resolution, the native resolution of land use and
238 LAI maps in GEOS-Chem. We calculated the relative change in forested area in the
239 scenarios for every 0.25° × 0.25° grid cell. The rainforest land use category in deforested
240 grid cells was correspondingly reduced by this factor, with the lost land area added to the
241 land use category for “Fields and Woody Savanna”. The LAI annual cycle for existing

242 Fields and Woody Savanna grid cells within the Amazon basin was spatially averaged
243 over 2003 and assigned to the deforested areas. Annual average LAI maps for the
244 Amazon scenarios used in GEOS-Chem are shown in Fig. S9. For these simulations, we
245 assumed that conversion of forest to agricultural land within the Amazon is fire-
246 mediated⁶⁶. Gridded biomass burning emissions were calculated by multiplying the
247 newly deforested areas for each year by mean fire Hg emissions ($380 \mu\text{g m}^{-2} \text{yr}^{-1}$) from
248 two observational studies in the Amazon^{19,67}. An additional 50% of the emissions (190
249 $\mu\text{g m}^{-2} \text{yr}^{-1}$) are released to the atmosphere within the first year as post-burn Hg⁰
250 emissions from soils¹⁸. To account for seasonal differences in meteorology and realistic
251 timing for forest clearing and burning⁶⁶, we assumed that deforestation occurs at the start
252 of June and deforestation biomass burning emissions occur in August and September .

253 The BAU and GOV scenarios do not account for any land-climate feedbacks²⁷, wherein
254 deforestation of the rainforest can lead to reduced moisture recycling and widespread
255 *savannization* (conversion of rainforest to savanna)⁶⁸. As an upper bound for this process,
256 we considered an extreme scenario (SAV) where the Amazon rainforest is fully
257 converted to savanna⁶⁹. The impact of this scenario on Hg⁰ deposition was previously
258 quantified²³, but here we reran the SAV simulation in GEOS-Chem to account for
259 updates in the soil Hg⁰ emissions parametrization. Fluxes for the Amazon region were
260 calculated by averaging over the area covered by the Soares-Filho et al.²⁷ deforestation
261 projections (shown in Fig. S8).

262 ***Potential reforestation scenario.*** We applied a reforestation scenario (RFR) in GEOS-
263 Chem based on the Global Reforestation Potential map^{30,70}, which considers the binary
264 potential of every 1 km^2 grid cell to be converted from non-forest (<25% tree cover in
265 2000–2009) to forest (>25% tree cover). The reforestation potential dataset does not
266 include areas that are native non-forest land cover types (e.g., grasslands) or cropland
267 areas. The reforestation potential was regridded to $0.25^\circ \times 0.25^\circ$ resolution. For every
268 grid cell where reforestation can occur, we identified the corresponding biome in the
269 Ecoregions2017 dataset⁴⁴ to determine the type of native forest vegetation that would
270 occur. If the corresponding biome of the grid cell was not a forest (e.g., coastal grid

271 cells), the most common forest type in the 8 neighboring grid cells was selected. The
272 added forest was assumed to have a LAI annual cycle equal to the 2003 spatial average
273 for all grid cells in the corresponding biome and biogeographic realm (LAI_{biome}). For grid
274 cells that were not a forest land type in 2003, we converted the reforested area fraction
275 (f_{rfr}) from the original land type to the new forest land type. Only grid cells where
276 LAI_{biome} is larger than the original land type LAI (LAI_{old}) were reforested. Since the land
277 map used in GEOS-Chem is at coarser resolution ($0.25^\circ \times 0.25^\circ$) than the reforestation
278 potential dataset ($1 \text{ km} \times 1 \text{ km}$), the reforested grid cell may already be a forest land type
279 in GEOS-Chem. In this case, we assumed that the grid cell LAI (LAI_{new}) will become
280 denser due to the new reforested area:

$$281 \quad LAI_{\text{new}} = LAI_{\text{old}} + f_{\text{rfr}} \cdot LAI_{\text{biome}} \quad (\text{Eq. 4})$$

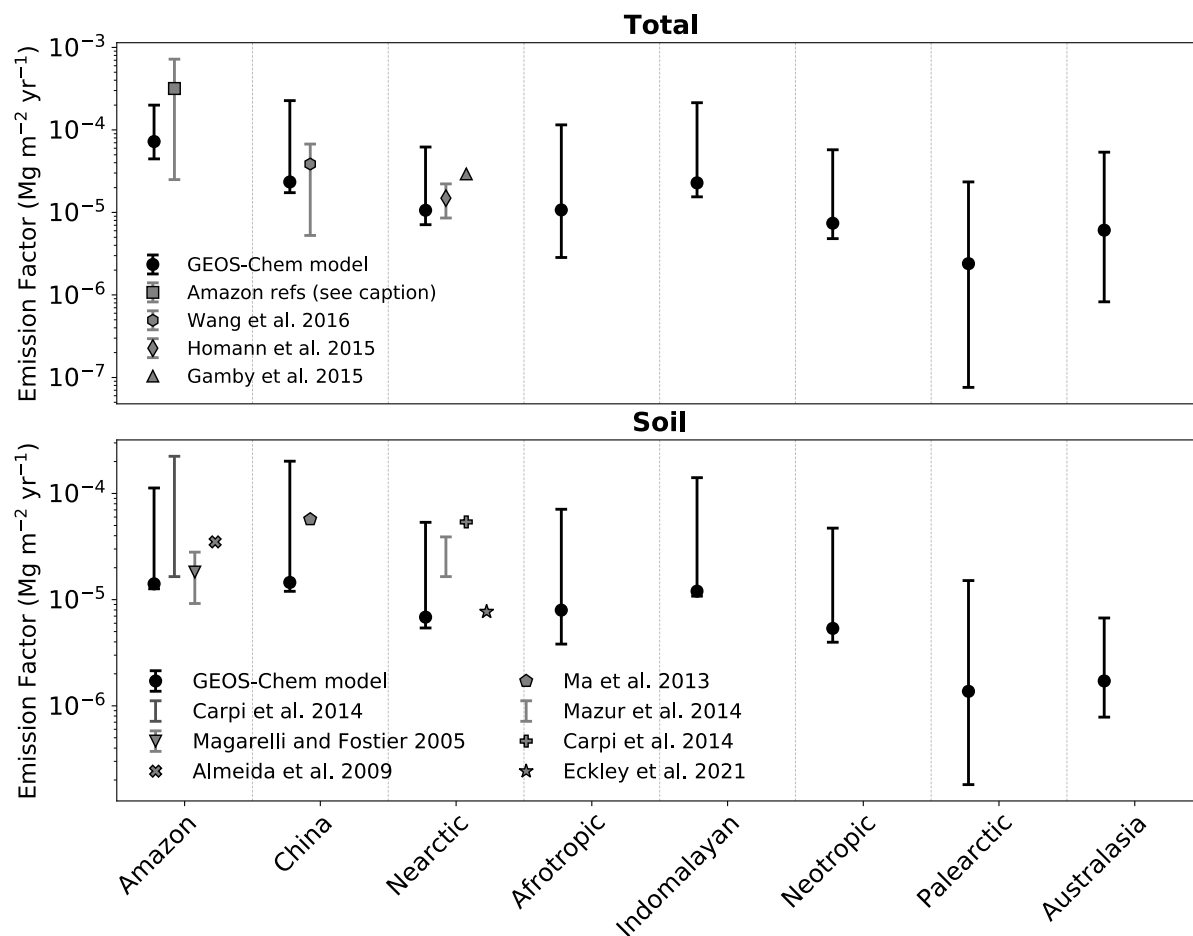
282 The resultant average LAI map in the RFR scenario is shown in Fig. S10.

283 **Uncertainty analysis.** We employed offline Python-based models for Hg^0 dry deposition
284 and soil Hg^0 emissions to estimate uncertainties in the simulated terrestrial-atmosphere
285 Hg fluxes from GEOS-Chem. These models are made publicly available for further reuse
286 (see Code and Data Availability). We focused on offline modeling of the Hg^0 dry
287 deposition and soil emissions as these processes contribute the overwhelming majority
288 (>98%) of the flux response to deforestation. The offline models contain the stand-alone
289 GEOS-Chem code for calculation of dry deposition velocities and soil emissions across
290 the horizontal model grid, but do not calculate atmospheric transport or chemical
291 transformations. Dry deposition fluxes of Hg^0 were calculated by multiplying the
292 deposition velocities by previously computed monthly Hg^0 concentration fields from the
293 online simulations. The offline models were run for the year 2015 using monthly average
294 diurnal cycles ($12 \times 24 \text{ h} = 288$ timesteps) of meteorological parameters, land surface
295 parameters, and Hg^0 concentration fields. At this time resolution, the offline models
296 showed sufficient accuracy compared to full online GEOS-Chem simulations, with
297 maximum errors compared to online predictions of 1% for annual mean soil emissions
298 and 5% for Hg^0 deposition. Given this level of accuracy and reduced computational
299 expense, the offline models are appropriate for estimating the parametric uncertainties in

300 atmosphere-terrestrial fluxes of the online GEOS-Chem model. We considered the
301 contributions of deposition parameters (f_0), soil emission parametrizations, the
302 assumption for LAI for replaced land types, and biomass burning emission factors (for
303 the Amazon simulations) to the overall uncertainty in fluxes. Uncertainty bounds of these
304 parameters are tabulated in Table S4. Latin Hypercube sampling⁷¹ was used to sample
305 100 parameter combinations. We conducted 100 simulations in the offline emissions and
306 deposition models for each studied scenario, calculating 95% confidence intervals from
307 the 2.5th and 97.5th percentile values in the offline calculated fluxes.

308 **Results and Discussion**

309 *Global estimate of deforestation-driven Hg fluxes.* To calculate net deforestation
310 emissions, we computed the difference in the net terrestrial-atmosphere exchange
311 (emissions from a grid cell minus deposition to a grid cell) before and after deforestation
312 (Eq. 3). For our global estimate of deforestation-driven emissions, we did not consider
313 immediate biomass burning emissions of Hg due to fire-mediated forest clearing nor
314 enhanced erosion fluxes, instead focusing on the impact on net Hg fluxes to the
315 atmosphere in the years after the clearing event. The major impacts to Hg fluxes arise
316 through enhanced soil Hg⁰ emissions and decreased Hg⁰ dry deposition due to reduced
317 canopy coverage, which can continue many years after the initial deforestation event^{18,61}.
318 Using perturbation simulations in GEOS-Chem for 8 global land regions, we calculated
319 regional emission factors (EFs) representing net fluxes to the atmosphere per unit
320 deforested area (in units Mg Hg m⁻² yr⁻¹).



321

322 **Figure 1.** Comparison between modeled and observation-derived net emission factors (EFs) for
 323 deforestation in different regions. The upper panel shows total EFs and the lower panel shows the
 324 soil Hg^0 emissions component of deforestation EFs. Modeled circles show the best estimate
 325 (online simulations), while error bars show the 95% confidence interval due to model parameter
 326 uncertainties (calculated in offline simulations, Section S4). Observation estimates are from
 327 refs.^{18,21,24,48-64}, with the Amazon Total EF estimate based on measurements in Fig. S3. Observed
 328 error bars refer to uncertainty ranges when multiple plots were measured within a study (further
 329 information about these calculations can be found in Section S2 and the SI Spreadsheet).

330

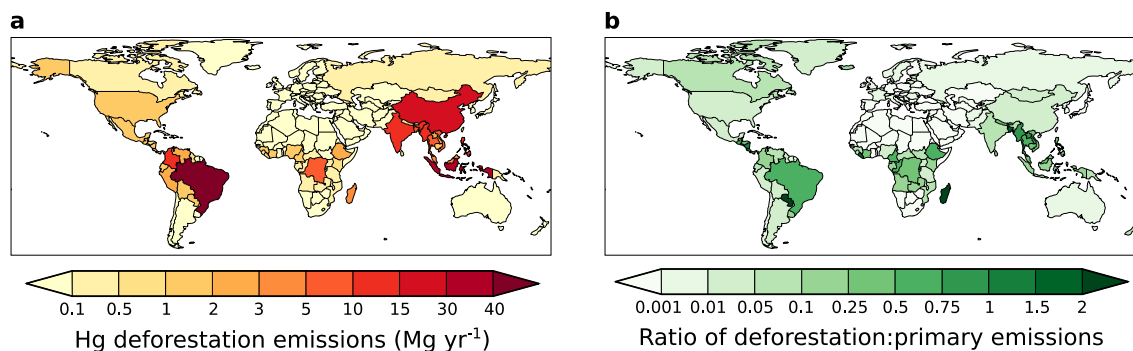
331 The calculated EFs are on the order of 10^{-6} to 10^{-4} $\text{Mg Hg m}^{-2} \text{ yr}^{-1}$ depending on the
 332 region (Fig. 1; Table S3), with the Amazon rainforest showing the highest EF (7×10^{-5}
 333 $\text{Mg Hg m}^{-2} \text{ yr}^{-1}$; 95% confidence interval, CI: 4×10^{-5} to 2×10^{-4} $\text{Mg Hg m}^{-2} \text{ yr}^{-1}$). This is
 334 to be expected from litterfall and throughfall measurements in the Amazon, which show
 335 some of the highest levels of Hg^0 vegetation uptake observed globally¹³, as well as Hg^0
 336 soil flux measurements from deforested areas in the Amazon, which show higher levels

337 of emissions compared to deforested North American soils¹⁸. The variation of simulated
338 EFs between regions depend on the factors that affect dry deposition (vegetation type and
339 LAI) and soil emission fluxes (LAI, soil Hg concentrations, and solar radiation). We
340 compiled available estimates of deforestation EFs from previous observational
341 studies^{18,21,24,48–64} and compared these to our modeled values (Fig. 1). Our EFs overlap
342 with available factors derived from observations, for the three regions where data are
343 available. The modeled error ranges appear well-calibrated as they cover a similar range
344 as the variability between observation-derived fluxes in the same region (Fig. 1). Fig. 1
345 also highlights that no observations of the impact of deforestation on Hg cycling are
346 currently available from the Afrotropic and Indomalayan regions, where deforestation is
347 widespread.

348 We multiplied the regional EFs by the deforested area from the CMIP6 Land-Use
349 Harmonization (LUH2) dataset⁴⁵ to calculate the net Hg fluxes to the atmosphere from
350 deforestation. Given the uncertain timescale for recovery in Hg sink capacity after
351 deforestation, we assumed that a deforested area has constant annual emissions over a
352 considered time horizon. Previous LULCC studies for carbon suggest that forests recover
353 their original biomass within 75 years after deforestation⁶⁵, so we employed time
354 horizons between 15–60 years (Fig. S6) to calculate 2015 deforestation-driven emissions.
355 In Fig. 2a, country-level deforestation emissions are shown based on a 45-year time
356 horizon (emissions released from areas deforested between 1970 and 2014). Net
357 emissions occurring in 2015 considering this 45-year deforestation time horizon are 217
358 Mg yr⁻¹ globally (CI: 134–1650 Mg yr⁻¹). Countries with substantial (>10 Mg yr⁻¹)
359 deforestation-driven emissions include Brazil (43 Mg yr⁻¹), Indonesia (35 Mg yr⁻¹), China
360 (16 Mg yr⁻¹), Colombia (14 Mg yr⁻¹), India (13 Mg yr⁻¹), Philippines (11 Mg yr⁻¹), and
361 Myanmar (11 Mg yr⁻¹). To put these emissions into context, Fig. 2b compares the
362 deforestation emissions with 2015 primary anthropogenic emissions inventory from
363 AMAP/UNEP^{9,38}. Deforestation Hg emissions are minor (<5%) compared to primary
364 anthropogenic emissions for most countries. However, for 32 countries, all located in the
365 tropics, deforestation emissions are greater than 30% of primary emissions. For Brazil,
366 which is the fifth highest emitter of primary Hg^{9,38}, deforestation emissions (43 Mg yr⁻¹)

367 are only 40% smaller than the 2015 emissions from primary anthropogenic sources (71
 368 Mg yr⁻¹). Deforestation emissions even exceed primary emissions in some countries,
 369 including Madagascar (deforestation emissions are 2.4× larger), Paraguay (2.3×), Liberia
 370 (2.0×), and Bangladesh (1.8×). Currently, Hg emissions inventories⁹ only consider
 371 primary anthropogenic emissions (2222 Mg yr⁻¹ in 2015), overlooking deforestation as a
 372 significant source of anthropogenic Hg to the atmosphere (217 Mg yr⁻¹). The relative
 373 importance of deforestation as an anthropogenic driver of Hg pollution could increase
 374 over the next decades, with primary anthropogenic emissions of Hg projected to halve to
 375 1020 Mg yr⁻¹ by 2035 under Minamata policies and reductions in fossil fuel use⁷².
 376 Therefore, assessing the potential impacts of land use policy scenarios will be crucial for
 377 predicting future Hg cycling, as primary anthropogenic emissions decline in the future.

378



379

380 **Figure 2.** Country-level annual deforestation emissions of Hg in 2015. (a) Deforestation-driven
 381 net emissions of Hg by country, assuming that deforested areas from the previous 45 years
 382 (1970–2014) contribute to emissions. (b) Ratio of deforestation emissions to primary
 383 anthropogenic emissions^{9,38} by country.

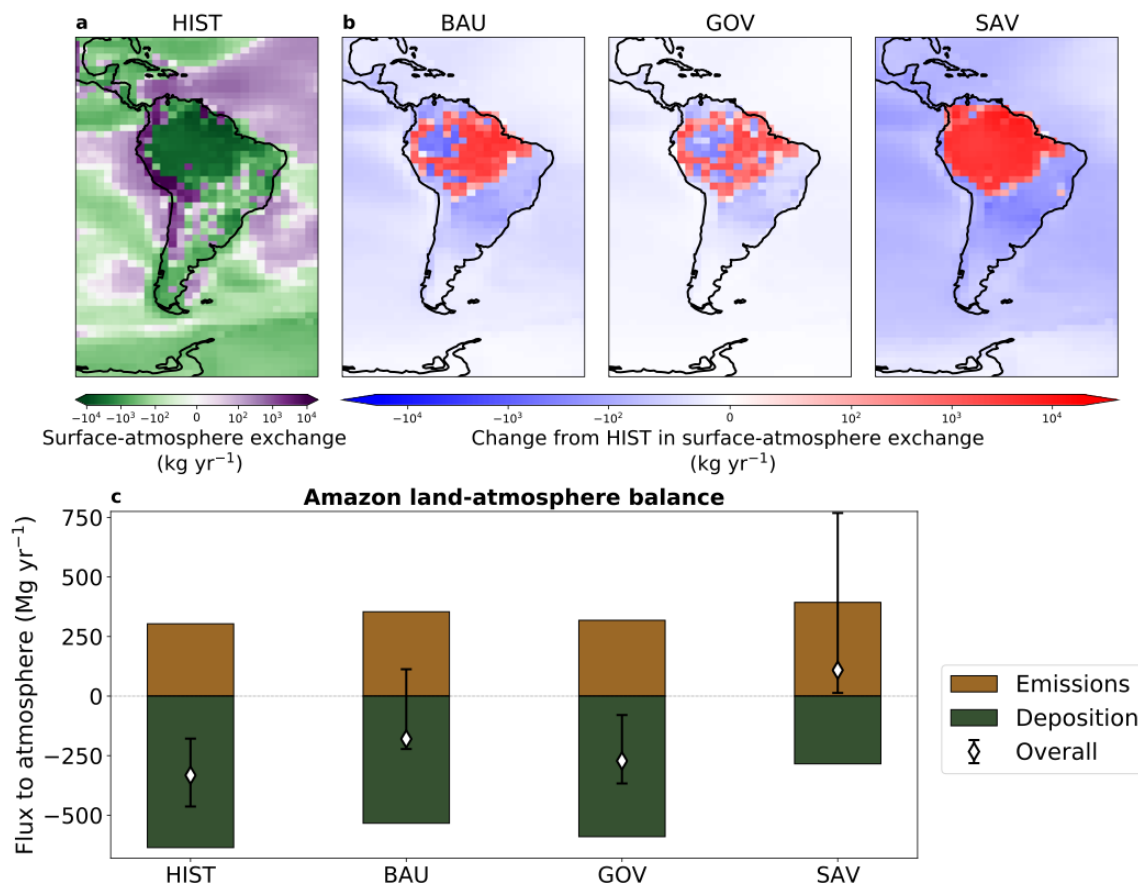
384

385 **Amazon conservation policy impacts on Hg cycling.** The Amazon is one of the regions
 386 with the highest Hg fluxes from deforestation (Fig. 2) and land policy choices will
 387 determine how this evolves in the future. Under historical forest coverage from 2003
 388 (HIST simulation), the Amazon rainforest stands out as a strong global sink of Hg (Fig.
 389 3a), with net input from the atmosphere to the rainforest totaling 332 Mg yr⁻¹ (CI: 179–
 390 463 Mg yr⁻¹). We studied the evolution of the Amazon Hg sink in two deforestation
 391 scenarios²⁷ for 2050: a business-as-usual scenario (BAU), which extrapolates historical
 392 deforestation tendencies into the future, and a governance scenario (GOV), which

393 assumes expanded conservation of the rainforest in the future. In the BAU scenario,
394 widespread deforestation, mainly in eastern Amazonia, reduces the net Hg inputs to soils
395 (Fig. 3b). While the Amazon region overall remains a net Hg sink in BAU, the removed
396 vegetation leads to decreased Hg^0 deposition in the Amazon (change from HIST: -105
397 Mg yr^{-1} ; CI: -53 to -152 Mg yr^{-1}) and enhanced Hg^0 emissions from soils ($+35 \text{ Mg yr}^{-1}$;
398 CI: 28 – 275 Mg yr^{-1}). For the Amazon policy scenarios, we have also considered the
399 impact that fire-mediated forest clearing^{66,73} has on biomass burning emissions of Hg,
400 which are 15 Mg yr^{-1} (CI: 10 – 17 Mg yr^{-1}) larger in BAU than HIST. The BAU scenario
401 shows atmospheric Hg^0 concentrations increasing up to 0.3 ng m^{-3} ($+50\%$) within the
402 Amazon region (Fig. S11); this would be a detectable change in Hg^0 , comparable to the
403 0.5 ng m^{-3} (-30%) decrease between 1995–2015 in North American Hg^0 observations⁷⁴.
404 The additional Hg fluxes from deforested areas can be transported over long distances in
405 the atmosphere and lead to more Hg deposition over oceans and remaining intact forest
406 areas (Fig. 3b). In the GOV scenario, deforestation is slowed by the conservation
407 measures, leading to smaller perturbations in the dry deposition flux from HIST (-47 Mg
408 yr^{-1} ; CI: -25 to -68 Mg yr^{-1}) and the soil emission flux ($+16 \text{ Mg yr}^{-1}$; CI: 12 – 126 Mg yr^{-1})
409 (Fig. 3b). In GOV, burning emissions from deforestation are 1 Mg yr^{-1} lower than in
410 HIST, due to lower annual rates of deforestation in the 2050 GOV scenario compared to
411 the HIST case representing 2003. Globally, the weakened rainforest sink of Hg yields
412 higher deposition of Hg to oceans compared to the reference simulation (BAU – HIST =
413 $+108 \text{ Mg yr}^{-1}$; GOV – HIST = $+44 \text{ Mg yr}^{-1}$).

414 Deforestation can be exacerbated through climate feedbacks, which are not considered in
415 these policy scenarios. For example, BAU projects that 40% of the Amazon will be
416 deforested by 2050²⁷, which could trigger a tipping point with widespread transition of
417 the rainforest to a savannah biome under diminished regional moisture recycling⁶⁸. To
418 evaluate this, we also re-ran an upper limit scenario from our previous work²³ where the
419 entire rainforest is converted to savannah (SAV). In this case, a strong decline in Hg^0 dry
420 deposition (-359 Mg yr^{-1} ; CI: -210 to -503 Mg yr^{-1}) and an increase in Hg^0 soil emissions
421 ($+89 \text{ Mg yr}^{-1}$; CI: 68 to 652 Mg yr^{-1}) drive enhanced inputs of Hg to the ocean (343 Mg
422 yr^{-1}) (Fig. 3b).

423 This change in the fate of atmospheric Hg (deposition to ocean instead of land) affects
424 both the spatial distribution and bioavailability of Hg pollution. When sequestered in
425 soils, Hg has an estimated residence time on the order of hundreds of years, whereas in
426 the surface ocean Hg is recycled to the atmosphere within months to years^{7,11}.
427 Deforestation thus increases the mobility of Hg by transferring Hg from locally-
428 sequestered reservoirs to the global pool. Human health risks are driven by exposure to
429 the more toxic form of the element, MeHg, which is produced through methylation in the
430 environment^{2,75}. Deforestation shifts Hg inputs from land to the ocean, where Hg can
431 more readily be methylated and bioaccumulate to dangerous levels in commercial fish.
432 Methylation and bioaccumulation of Hg can also occur in forested soils, but MeHg levels
433 in aquatic ecosystems are generally much higher (overall global ocean average = 15%)⁷⁶
434 than in Amazonian soils (1–5%)^{48,77}. In addition, the long length of aquatic food chains
435 leads to high levels of MeHg in commonly consumed fish species at higher trophic levels
436 (e.g., tuna, cod, and swordfish)⁷⁵.



437

438 **Figure 3.** Impacts of Amazon deforestation scenarios on surface-atmosphere Hg exchange. (a)
 439 The simulated surface-atmosphere exchange (net deposition is negative and net emission is
 440 positive) of Hg in the reference simulation (HIST). (b) Changes in exchange fluxes from HIST
 441 are shown for the deforestation scenarios: Business-as-usual (BAU), Governance (GOV), and
 442 Savannization (SAV); negative values refer to increased net fluxes to the surface compared to
 443 HIST and positive values refer to increased net fluxes to the atmosphere. (c) Total simulated
 444 fluxes of Hg emissions and deposition are calculated for the Amazon region in each scenario.
 445 White diamonds illustrate the net flux of Hg to the atmosphere (= emissions – deposition) and
 446 error bars refer to the 95% confidence interval based on model parameter uncertainties.

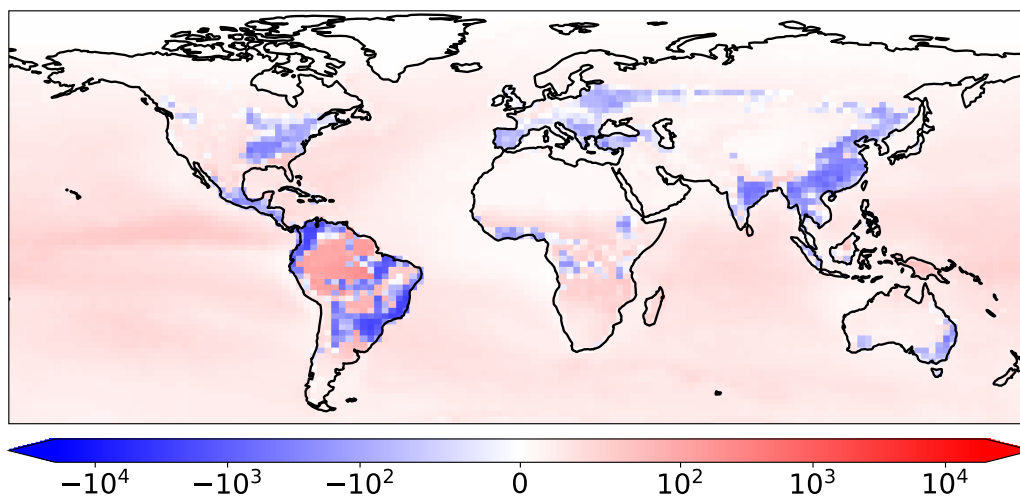
447

448 Deforestation policy substantially impacts the soil mass balance of Hg in the Amazon
 449 region, illustrated by our modeling simulations (Fig. 3c) and available field observations
 450 (Fig. S3). If agricultural expansion continues as in BAU, the net Amazon sink of
 451 atmospheric Hg is weakened by 153 Mg yr⁻¹ (CI: 97–418 Mg yr⁻¹) (Fig. 3c). The
 452 reduction of forest Hg⁰ uptake contributes two-thirds of the net flux response in the BAU
 453 scenario, while increases in emissions contribute the remaining third. Under the more
 454 moderate GOV scenario, the Amazon Hg sink (272 Mg yr⁻¹; CI: 79–367 Mg yr⁻¹) is better

455 preserved, though still 18% (CI: 14–65%) smaller than HIST. Stricter conservation
456 policies in GOV yield an additional 92 Mg yr⁻¹ (CI: 59–234 Mg yr⁻¹) of Hg sequestered in
457 the Amazon compared to BAU. The SAV scenario illustrates that additional climate
458 feedbacks could flip the Amazon from a net Hg sink to a source (+109 Mg yr⁻¹; CI: 13–
459 768 Mg yr⁻¹). These Hg projections parallel recent findings on Amazon carbon cycling,
460 which have demonstrated that climate change and deforestation are turning the Amazon
461 into a CO₂ source²⁵. In addition to atmosphere-terrestrial exchange fluxes, soil erosion of
462 Hg can also be altered due to deforestation. We applied a soil erosion model GloSEM^{78,79}
463 to evaluate the impact of deforestation on erosion in the Amazon basin (Supplementary
464 Information Section S6). In terms of Hg flux magnitudes, perturbations to erosion are
465 smaller (<15%) than changes to the atmosphere-terrestrial exchange fluxes (Section S6),
466 which is supported by field studies⁶⁴. Nevertheless, deforestation also enhances Hg
467 erosion in both scenarios (BAU: +33%; GOV: +14%), accelerating the transfer of
468 terrestrial Hg to aquatic ecosystems.

469 ***Quantifying the Hg mitigation potential of reforestation.*** Reforestation has been
470 identified as a potential mitigation approach for climate change, by strengthening the
471 terrestrial CO₂ sink^{30,80}. To investigate the concurrent strengthening of the terrestrial Hg
472 sink and the impacts on Hg cycling, we considered a global reforestation scenario (RFR)
473 based on the Global Reforestation Potential Map^{30,70}, which identified areas suitable for
474 reforestation worldwide (i.e., not including croplands or areas where forests are not
475 native). Figure 4 maps the impacts of reforestation on Hg surface-atmosphere exchange,
476 comparing to the reference HIST simulation. The spatial distribution of reforestation
477 impacts depends both on the areal extent of reforestation as well as the reforested
478 vegetation type. Net deposition of Hg increases over reforested areas (blue areas in Fig.
479 4), while net deposition declines over the ocean as well as land areas with existing forests
480 (red areas in Fig. 4). Globally, RFR enhances uptake of Hg on land by 98 Mg yr⁻¹ (CI:
481 64–449 Mg yr⁻¹) compared to HIST, thereby reducing Hg deposition to oceans.
482 Reforestation could thus take up approximately 5% of the anthropogenic Hg emission
483 flux (~2200 Mg yr⁻¹)⁹. In addition to the targeted benefits for biodiversity and climate
484 change mitigation³⁰, reforestation could moderately reduce levels of Hg in marine

485 ecosystems, and thus commercial fish. Nevertheless, the magnitude of reforestation
 486 impact (5% of primary emissions) illustrates that reforestation is not a substitute for
 487 implementing extensive cuts to primary Hg emissions, like in the CO₂ context²⁹.



Reforestation change in surface-atmosphere exchange (kg yr^{-1})

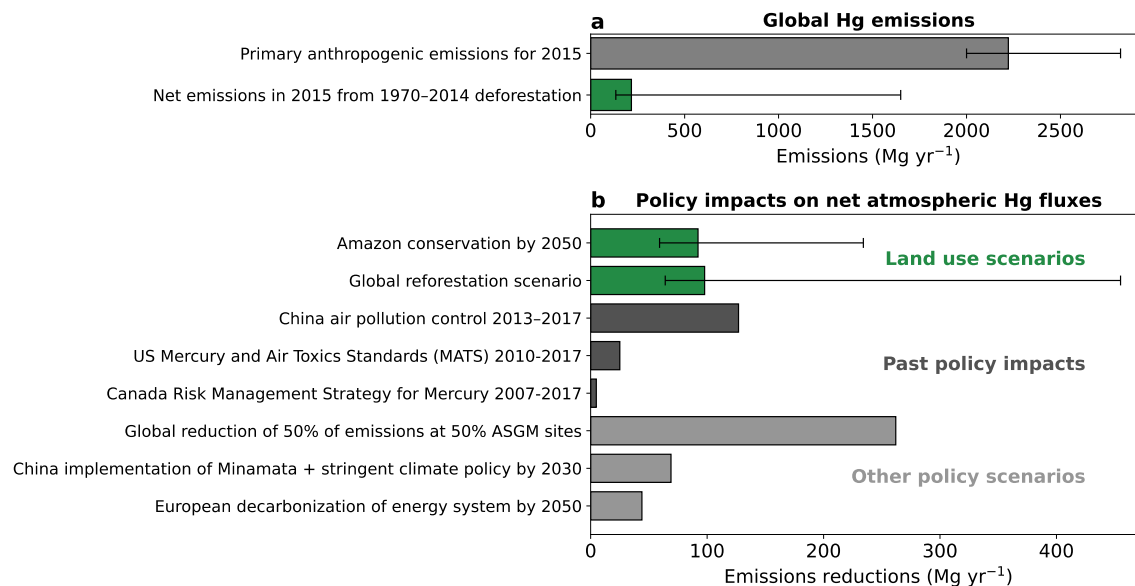
488 **Figure 4.** Enhanced land sink of Hg with reforestation. The impact of the potential reforestation
 489 (RFR) scenario on surface-atmosphere exchange. The differences from the reference (HIST)
 490 simulation are shown, with negative values referring to increased net fluxes to the surface and
 491 positive values referring to decreased net fluxes to the surface.
 492
 493

494 Potential reforestation opportunities for Hg are dominated by the Amazon and Atlantic
 495 forest regions in South America (71 Mg yr^{-1} , 72% of total land sink impact) (Fig. 4). The
 496 potential reforestation impact on atmospheric fluxes in Northern extratropical areas alone
 497 (-29 Mg yr^{-1}) would not compensate for increased Hg emissions due to deforestation in
 498 the Amazon (BAU: $+153 \text{ Mg yr}^{-1}$; GOV: $+61 \text{ Mg yr}^{-1}$). Overall, more information would
 499 be needed to compare the potentials of reforestation and conservation policies on a global
 500 scale, as the deforestation policy scenarios focused only on a specific region (the
 501 Amazon); future research could study conservation impacts in other tropical regions with
 502 high Hg deforestation emissions (Fig. 2) (e.g., in Africa and Southeast Asia). Our
 503 simulated fluxes consider the uptake of Hg upon maturation of forest stands, as reforested
 504 areas are assumed to have LAI of existent corresponding biomes. Further experimental

505 research would be required to understand the transient response of Hg uptake during the
506 growth of forests.

507 ***Limitations of modeling approach.*** The current work provides an initial assessment of
508 the global emissions of Hg from deforestation, which can spur future investigation into
509 the impact of LULCC on Hg. Other LULCC processes (e.g., wood harvest and
510 agricultural practices) may also affect Hg fluxes but have not been considered within this
511 study. As well, due to the early stage of Hg research, there is not yet the same level of
512 information for Hg that is commonly included in LULCC assessments for carbon,
513 including temporal information on the release of Hg from soils and Hg uptake rates
514 during regrowth of vegetation²². Although we have assembled a dataset of available
515 deforestation flux measurements covering multiple regions (SI Spreadsheet), there
516 continues to be a lack of measurements in relevant regions (e.g., Afrotropic and
517 Indomalayan) to constrain the response of Hg fluxes to deforestation, contributing
518 uncertainty to this work. As information from field measurements becomes more
519 available, it will be possible for future modeling studies to analyze smaller sub-regions
520 differentiated by ecosystem types, improving the accuracy of deforestation-driven
521 emissions. In the current work, the parametrization of Hg⁰ soil emissions is based on
522 solar radiation and soil Hg concentration, which is the current state of the art for global
523 models and in agreement with available flux measurements (Fig. 1). Field
524 observations^{81,82} have investigated the role of other environmental parameters including
525 precipitation, soil moisture, soil chemistry, soil physics, and microbial interactions, along
526 with anthropogenic factors such as emissions from directly contaminated soils⁸³ that
527 would not be captured at the resolution of the global modeling approach. Regional
528 models of Hg⁰ soil emissions include a wider array of these parameters²⁴, but further
529 research would be required to produce a tuned parametrization of this complexity at the
530 global scale. The development of terrestrial Hg cycles and LULCC processes within
531 Earth system models⁸⁴ will be vital to investigate the evolution of the Hg land sink over
532 time and the effect on environmental Hg risks.

533 ***Implications for global Hg policy.*** Land use policy has been largely unexplored as a
534 lever to mitigate Hg pollution. On the global scale, the estimated deforestation-driven Hg
535 emissions in 2015 (217 Mg yr⁻¹; CI: 134–1650 Mg yr⁻¹) correspond to 10% of the global
536 primary anthropogenic emissions⁹ (2222 Mg yr⁻¹) (Fig. 5a). Therefore, though cutting
537 primary anthropogenic emissions remains a priority, deforestation fluxes should not be
538 overlooked in assessments of Hg pollution, especially for countries in the tropics (Fig.
539 2b). The potential of Amazon conservation and global reforestation to reduce net Hg
540 emissions in the future is substantial compared to previously quantified policies aimed at
541 tackling primary anthropogenic emissions (Fig. 5b). Potential emissions reductions from
542 Amazon conservation (92 Mg yr⁻¹) and global reforestation (98 Mg yr⁻¹) are within the
543 range of impacts of past policy and future policy scenarios aimed at reducing Hg from
544 specific anthropogenic sources or due to national climate and air pollution policies (5–
545 262 Mg yr⁻¹)^{85–90}. Emissions reductions from land use policies are different from primary
546 emissions reductions in that their efficacy depends on whether the storage of Hg in soils
547 is over a long-term period. Similar to CO₂, the potential benefits of enhanced Hg uptake
548 on land can be reversed by human or natural disturbances, e.g., by climate change
549 increasing the frequency of wildfires — which re-emit Hg and carbon from terrestrial
550 ecosystems — and droughts — which reduce Hg and CO₂ uptake by plants^{30,91}. Thus,
551 mitigation of Hg pollution by conserving and increasing forest area can only be realized
552 with concurrent efforts to sustainably manage land areas and preventing severe climate
553 change. The potential of sustainable land use to mitigate Hg pollution could enable
554 collaborations between the Minamata Convention and other global policy efforts to
555 reduce deforestation, e.g., the 2021 Glasgow Declaration⁹². Ultimately, mitigation of
556 global Hg pollution depends not only on reducing primary anthropogenic emissions, but
557 also reducing anthropogenic activities like deforestation that re-mobilize legacy Hg.



558 **Figure 5.** Potential of land use policies to reduce net Hg fluxes to the atmosphere. (a) Comparing
 559 global 2015 emissions from primary anthropogenic emissions^{9,38} and deforestation-driven
 560 emissions, assuming a 45-year time horizon (1970–2014 deforested areas). (b) Net Hg emissions
 561 reductions from land use policies (this study) are compared to primary anthropogenic emissions
 562 policies, whose impacts have been quantified in the literature^{85–90}. ASGM refers to artisanal and
 563 small-scale gold mining. For land use scenarios, “Amazon conservation by 2050” refers to the net
 564 emissions reductions in the 2050 governance (GOV) from the business-as-usual (BAU)
 565 simulations and “Global reforestation scenario” compares the net emissions reductions in the
 566 reforestation scenario (RFR) compared to the reference simulation (HIST). Error bars for this
 567 study refer to the 95% confidence interval based on model parameter uncertainties.
 568

569

570 Acknowledgments

571 This work was funded by the Swiss National Science Foundation through an Early
 572 Postdoc.Mobility grant to A.F. (P2EZP2_195424) and an Ambizione grant to M.J.
 573 (PZ00P2_174101), a grant (#1924148) from the US National Science Foundation to
 574 N.E.S., and an Academic Transition Grant from Eawag to J.B. We thank Ronny Meier
 575 and Michael Windisch for assistance in processing the reforestation potential dataset. We
 576 thank Luiz D. Lacerda for sharing Hg data from Brazil. We acknowledge all researchers
 577 involved in conducting field studies measuring the impact of deforestation on Hg fluxes.

578

579

580

581 **Code and Data Availability**

582 Model code, analysis scripts, and simulation data supporting the results of this study are
583 published in Zenodo (<https://doi.org/10.5281/zenodo.8364698>) under a CC BY 4.0
584 license (<https://creativecommons.org/licenses/by/4.0/>).

585

586 **Associated Content**

587 **Supporting Information.** Further supporting information can be found in the following
588 files:

589 Soil emissions parametrization; Observations of deforestation fluxes; Global
590 deforestation-driven emissions estimates; Parameters for uncertainty analysis;
591 Scenario maps; Erosion calculations; Atmospheric concentration impacts (PDF)

592

593 Tabulated dataset of literature Hg deforestation flux measurements (XLSX)

594

595 **Author Contributions**

596 All authors conceived the study. M.J., J.B., and A.F. compiled Hg field data through
597 literature review. A.F. and P.B performed the simulations. All authors contributed to the
598 data analysis. A.F. wrote the draft of the paper with contributions and revisions from all
599 authors.

600

601 **References**

- 602 (1) Sheehan, M. C.; Burke, T. A.; Navas-Acien, A.; Breyse, P. N.; McGready, J.; Fox, M. A.
603 Global Methylmercury Exposure from Seafood Consumption and Risk of Developmental
604 Neurotoxicity: A Systematic Review. *Bull. World Health Organ.* **2014**, *92* (4), 254-269F.
605 <https://doi.org/10.2471/BLT.12.116152>.
- 606 (2) Zhang, Y.; Song, Z.; Huang, S.; Zhang, P.; Peng, Y.; Wu, P.; Gu, J.; Dutkiewicz, S.; Zhang,
607 H.; Wu, S.; Wang, F.; Chen, L.; Wang, S.; Li, P. Global Health Effects of Future
608 Atmospheric Mercury Emissions. *Nat Commun* **2021**, *12* (1), 3035.
609 <https://doi.org/10.1038/s41467-021-23391-7>.
- 610 (3) Bellanger, M.; Pichery, C.; Aerts, D.; Berglund, M.; Castaño, A.; Čejchanová, M.; Crettaz,
611 P.; Davidson, F.; Esteban, M.; Fischer, M. E.; Gurzau, A. E.; Halzlova, K.; Katsonouri, A.;
612 Knudsen, L. E.; Kolossa-Gehring, M.; Koppen, G.; Ligočka, D.; Miklavčič, A.; Reis, M. F.;
613 Rudnai, P.; Tratnik, J. S.; Weihe, P.; Budtz-Jørgensen, E.; Grandjean, P.; DEMO/COPHES.
614 Economic Benefits of Methylmercury Exposure Control in Europe: Monetary Value of

- 615 Neurotoxicity Prevention. *Environ Health* **2013**, *12* (1), 3. [https://doi.org/10.1186/1476-](https://doi.org/10.1186/1476-069X-12-3)
616 069X-12-3.
- 617 (4) Outridge, P. M.; Mason, R. P.; Wang, F.; Guerrero, S.; Heimbürger-Boavida, L. E. Updated
618 Global and Oceanic Mercury Budgets for the United Nations Global Mercury Assessment
619 2018. *Environ. Sci. Technol.* **2018**, *acs.est.8b01246*.
620 <https://doi.org/10.1021/acs.est.8b01246>.
- 621 (5) Shah, V.; Jacob, D. J.; Thackray, C. P.; Wang, X.; Sunderland, E. M.; Dibble, T. S.; Saiz-
622 Lopez, A.; Černušák, I.; Kellö, V.; Castro, P. J.; Wu, R.; Wang, C. Improved Mechanistic
623 Model of the Atmospheric Redox Chemistry of Mercury. *Environ. Sci. Technol.* **2021**, *55*
624 (21), 14445–14456. <https://doi.org/10.1021/acs.est.1c03160>.
- 625 (6) UNTC. *Minamata Convention on Mercury*; 2013.
626 [https://treaties.un.org/Pages/ViewDetails.aspx?src=TREATY&mtdsg_no=XXVII-](https://treaties.un.org/Pages/ViewDetails.aspx?src=TREATY&mtdsg_no=XXVII-17&chapter=27)
627 17&chapter=27.
- 628 (7) Amos, H. M.; Jacob, D. J.; Streets, D. G.; Sunderland, E. M. Legacy Impacts of All-Time
629 Anthropogenic Emissions on the Global Mercury Cycle. *Global Biogeochem. Cycles* **2013**,
630 *27* (2), 410–421. <https://doi.org/10.1002/gbc.20040>.
- 631 (8) Zhou, J.; Obrist, D.; Dastoor, A.; Jiskra, M.; Ryjkov, A. Vegetation Uptake of Mercury and
632 Impacts on Global Cycling. *Nat. Rev. Earth Environ.* **2021**, *2* (4), 269–284.
633 <https://doi.org/10.1038/s43017-021-00146-y>.
- 634 (9) UNEP. *Global Mercury Assessment 2018*; UN Environment Programme, Chemicals and
635 Health Branch. Geneva, Switzerland, 2019.
- 636 (10) Schaefer, K.; Elshorbany, Y.; Jafarov, E.; Schuster, P. F.; Striegl, R. G.; Wickland, K. P.;
637 Sunderland, E. M. Potential Impacts of Mercury Released from Thawing Permafrost. *Nat*
638 *Commun* **2020**, *11* (1), 4650. <https://doi.org/10.1038/s41467-020-18398-5>.
- 639 (11) Smith-Downey, N. V.; Sunderland, E. M.; Jacob, D. J. Anthropogenic Impacts on Global
640 Storage and Emissions of Mercury from Terrestrial Soils: Insights from a New Global
641 Model. *J. Geophys. Res.* **2010**, *115* (G3), G03008. <https://doi.org/10.1029/2009JG001124>.
- 642 (12) Jiskra, M.; Sonke, J. E.; Obrist, D.; Bieser, J.; Ebinghaus, R.; Myhre, C. L.; Pfaffhuber, K.
643 A.; Wängberg, I.; Kyllönen, K.; Worthy, D.; Martin, L. G.; Labuschagne, C.; Mkololo, T.;
644 Ramonet, M.; Magand, O.; Dommergue, A. A Vegetation Control on Seasonal Variations in
645 Global Atmospheric Mercury Concentrations. *Nature Geosci* **2018**, *11* (4), 244–250.
646 <https://doi.org/10.1038/s41561-018-0078-8>.
- 647 (13) Fostier, A. H.; Melendez-Perez, J. J.; Richter, L. Litter Mercury Deposition in the
648 Amazonian Rainforest. *Environ. Pollut.* **2015**, *206*, 605–610.
649 <https://doi.org/10.1016/j.envpol.2015.08.010>.
- 650 (14) IPCC. *Climate Change and Land: An IPCC Special Report on Climate Change,*
651 *Desertification, Land Degradation, Sustainable Land Management, Food Security, and*
652 *Greenhouse Gas Fluxes in Terrestrial Ecosystems*; Shukla, P. R., Skeg, J., Calvo Buendia,
653 E., Masson-Delmotte, V., Pörtner, H.-O., Roberts, D. C., Zhai, P., Slade, R., Connors, S.,
654 van Diemen, S., Ferrat, M., Haughey, E., Luz, S., Pathak, M., Petzold, J., Portugal Pereira,
655 J., Vyas, P., Huntley, E., Kissick, K., Belkacemi, M., Malley, J., Eds.; 2019.
- 656 (15) Zhang, H.; Holmes, C. D.; Wu, S. Impacts of Changes in Climate, Land Use and Land
657 Cover on Atmospheric Mercury. *Atmos. Environ.* **2016**, *141*, 230–244.
658 <https://doi.org/10.1016/j.atmosenv.2016.06.056>.
- 659 (16) UNFCCC. *The Paris Agreement*; 2015. [https://unfccc.int/process-and-meetings/the-paris-](https://unfccc.int/process-and-meetings/the-paris-agreement/the-paris-agreement)
660 agreement/the-paris-agreement.
- 661 (17) Adler Miserendino, R.; Guimarães, J. R. D.; Schudel, G.; Ghosh, S.; Godoy, J. M.;
662 Silbergeld, E. K.; Lees, P. S. J.; Bergquist, B. A. Mercury Pollution in Amapá, Brazil:
663 Mercury Amalgamation in Artisanal and Small-Scale Gold Mining or Land-Cover and

- 664 Land-Use Changes? *ACS Earth Space Chem.* **2018**, 2 (5), 441–450.
665 <https://doi.org/10.1021/acsearthspacechem.7b00089>.
- 666 (18) Carpi, A.; Fostier, A. H.; Orta, O. R.; dos Santos, J. C.; Gittings, M. Gaseous Mercury
667 Emissions from Soil Following Forest Loss and Land Use Changes: Field Experiments in
668 the United States and Brazil. *Atmos. Environ.* **2014**, 96, 423–429.
669 <https://doi.org/10.1016/j.atmosenv.2014.08.004>.
- 670 (19) Melendez-Perez, J. J.; Fostier, A. H.; Carvalho, J. A.; Windmüller, C. C.; Santos, J. C.;
671 Carpi, A. Soil and Biomass Mercury Emissions during a Prescribed Fire in the Amazonian
672 Rain Forest. *Atmospheric Environment* **2014**, 96, 415–422.
673 <https://doi.org/10.1016/j.atmosenv.2014.06.032>.
- 674 (20) Roulet, M.; Lucotte, M.; Farella, N.; Serique, G.; Coelho, H.; Passos, S.; Mergler, D.
675 Effects of Recent Human Colonization on the Presence of Mercury in Amazonian
676 Ecosystems. *Water Air Soil Pollut.* **1999**, 112, 297–313.
- 677 (21) Fostier, A. H.; Forti, M. C.; Guimarães, J. R.; Melfi, A. J.; Boulet, R.; Espirito Santo, C. M.;
678 Krug, F. J. Mercury Fluxes in a Natural Forested Amazonian Catchment (Serra Do Navio,
679 Amapá State, Brazil). *Sci. Total Environ.* **2000**, 260 (1–3), 201–211.
680 [https://doi.org/10.1016/S0048-9697\(00\)00564-7](https://doi.org/10.1016/S0048-9697(00)00564-7).
- 681 (22) Obermeier, W. A.; Nabel, J. E. M. S.; Loughran, T.; Hartung, K.; Bastos, A.; Havermann,
682 F.; Anthoni, P.; Arneith, A.; Goll, D. S.; Lienert, S.; Lombardozzi, D.; Luysaert, S.;
683 McGuire, P. C.; Melton, J. R.; Poulter, B.; Sitch, S.; Sullivan, M. O.; Tian, H.; Walker, A.
684 P.; Wiltshire, A. J.; Zaehle, S.; Pongratz, J. Modelled Land Use and Land Cover Change
685 Emissions – a Spatio-Temporal Comparison of Different Approaches. *Earth Syst. Dynam.*
686 **2021**, 12 (2), 635–670. <https://doi.org/10.5194/esd-12-635-2021>.
- 687 (23) Feinberg, A.; Dlamini, T.; Jiskra, M.; Shah, V.; Selin, N. E. Evaluating Atmospheric
688 Mercury (Hg) Uptake by Vegetation in a Chemistry-Transport Model. *Environ. Sci.:
689 Processes Impacts* **2022**, 24 (9), 1303–1318. <https://doi.org/10.1039/D2EM00032F>.
- 690 (24) Wang, X.; Lin, C.-J.; Yuan, W.; Sommar, J.; Zhu, W.; Feng, X. Emission-Dominated Gas
691 Exchange of Elemental Mercury Vapor over Natural Surfaces in China. *Atmos. Chem. Phys.*
692 **2016**, 16 (17), 11125–11143. <https://doi.org/10.5194/acp-16-11125-2016>.
- 693 (25) Gatti, L. V.; Basso, L. S.; Miller, J. B.; Gloor, M.; Gatti Domingues, L.; Cassol, H. L. G.;
694 Tejada, G.; Aragão, L. E. O. C.; Nobre, C.; Peters, W.; Marani, L.; Arai, E.; Sanches, A. H.;
695 Corrêa, S. M.; Anderson, L.; Von Randow, C.; Correia, C. S. C.; Crispim, S. P.; Neves, R.
696 A. L. Amazonia as a Carbon Source Linked to Deforestation and Climate Change. *Nature*
697 **2021**, 595 (7867), 388–393. <https://doi.org/10.1038/s41586-021-03629-6>.
- 698 (26) Tyukavina, A.; Hansen, M. C.; Potapov, P. V.; Stehman, S. V.; Smith-Rodriguez, K.; Okpa,
699 C.; Aguilar, R. Types and Rates of Forest Disturbance in Brazilian Legal Amazon, 2000–
700 2013. *Sci. Adv.* **2017**, 3 (4), e1601047. <https://doi.org/10.1126/sciadv.1601047>.
- 701 (27) Soares-Filho, B. S.; Nepstad, D. C.; Curran, L. M.; Cerqueira, G. C.; Garcia, R. A.; Ramos,
702 C. A.; Voll, E.; McDonald, A.; Lefebvre, P.; Schlesinger, P. Modelling Conservation in the
703 Amazon Basin. *Nature* **2006**, 440 (7083), 520–523. <https://doi.org/10.1038/nature04389>.
- 704 (28) IPCC. Summary for Policymakers. In *Climate Change 2022: Mitigation of Climate Change.
705 Contribution of Working Group III to the Sixth Assessment Report of the Intergovernmental
706 Panel on Climate Change*; [P.R. Shukla, J. Skea, R. Slade, A. Al Khourdjie, R. van
707 Diemen, D. McCollum, M. Pathak, S. Some, P. Vyas, R. Fradera, M. Belkacemi, A. Hasija,
708 G. Lisboa, S. Luz, J. Malley, (eds.)]. Cambridge University Press, Cambridge, UK and New
709 York, NY, USA.
- 710 (29) Holl, K. D.; Brancalion, P. H. S. Tree Planting Is Not a Simple Solution. *Science* **2020**, 368
711 (6491), 580–581. <https://doi.org/10.1126/science.aba8232>.

- 712 (30) Griscom, B. W.; Adams, J.; Ellis, P. W.; Houghton, R. A.; Lomax, G.; Miteva, D. A.;
713 Schlesinger, W. H.; Shoch, D.; Siikamäki, J. V.; Smith, P.; Woodbury, P.; Zganjar, C.;
714 Blackman, A.; Campari, J.; Conant, R. T.; Delgado, C.; Elias, P.; Gopalakrishna, T.;
715 Hamsik, M. R.; Herrero, M.; Kiesecker, J.; Landis, E.; Laestadius, L.; Leavitt, S. M.;
716 Minnemeyer, S.; Polasky, S.; Potapov, P.; Putz, F. E.; Sanderman, J.; Silvius, M.;
717 Wollenberg, E.; Fargione, J. *Natural Climate Solutions. Proc. Natl. Acad. Sci. U.S.A.* **2017**,
718 *114* (44), 11645–11650. <https://doi.org/10.1073/pnas.1710465114>.
- 719 (31) Gelaro, R.; McCarty, W.; Suárez, M. J.; Todling, R.; Molod, A.; Takacs, L.; Randles, C. A.;
720 Darmenov, A.; Bosilovich, M. G.; Reichle, R.; Wargan, K.; Coy, L.; Cullather, R.; Draper,
721 C.; Akella, S.; Buchard, V.; Conaty, A.; Silva, A. M. da; Gu, W.; Kim, G.-K.; Koster, R.;
722 Lucchesi, R.; Merkova, D.; Nielsen, J. E.; Partyka, G.; Pawson, S.; Putman, W.; Rienecker,
723 M.; Schubert, S. D.; Sienkiewicz, M.; Zhao, B. The Modern-Era Retrospective Analysis for
724 Research and Applications, Version 2 (MERRA-2). *J. Clim.* **2017**, *30* (14), 5419–5454.
725 <https://doi.org/10.1175/JCLI-D-16-0758.1>.
- 726 (32) Horowitz, H. M.; Jacob, D. J.; Zhang, Y.; Dibble, T. S.; Slemr, F.; Amos, H. M.; Schmidt,
727 J. A.; Corbitt, E. S.; Marais, E. A.; Sunderland, E. M. A New Mechanism for Atmospheric
728 Mercury Redox Chemistry: Implications for the Global Mercury Budget. *Atmos. Chem.*
729 *Phys.* **2017**, *17* (10), 6353–6371. <https://doi.org/10.5194/acp-17-6353-2017>.
- 730 (33) Amos, H. M.; Jacob, D. J.; Holmes, C. D.; Fisher, J. A.; Wang, Q.; Yantosca, R. M.;
731 Corbitt, E. S.; Galarneau, E.; Rutter, A. P.; Gustin, M. S.; Steffen, A.; Schauer, J. J.;
732 Graydon, J. A.; Louis, V. L. St.; Talbot, R. W.; Edgerton, E. S.; Zhang, Y.; Sunderland, E.
733 M. Gas-Particle Partitioning of Atmospheric Hg(II) and Its Effect on Global Mercury
734 Deposition. *Atmos. Chem. Phys.* **2012**, *12* (1), 591–603. [https://doi.org/10.5194/acp-12-591-](https://doi.org/10.5194/acp-12-591-2012)
735 [2012](https://doi.org/10.5194/acp-12-591-2012).
- 736 (34) Wang, Y.; Jacob, D. J.; Logan, J. A. Global Simulation of Tropospheric O₃-NO_x-
737 Hydrocarbon Chemistry: 1. Model Formulation. *J. Geophys. Res.* **1998**, *103* (D9), 10713–
738 10725. <https://doi.org/10.1029/98JD00158>.
- 739 (35) Fisher, J. A.; Jacob, D. J.; Wang, Q.; Bahreini, R.; Carouge, C. C.; Cubison, M. J.; Dibb, J.
740 E.; Diehl, T.; Jimenez, J. L.; Leibensperger, E. M.; Lu, Z.; Meinders, M. B. J.; Pye, H. O.
741 T.; Quinn, P. K.; Sharma, S.; Streets, D. G.; van Donkelaar, A.; Yantosca, R. M. Sources,
742 Distribution, and Acidity of Sulfate–Ammonium Aerosol in the Arctic in Winter–Spring.
743 *Atmos. Environ.* **2011**, *45* (39), 7301–7318. <https://doi.org/10.1016/j.atmosenv.2011.08.030>.
- 744 (36) Gibbs, H. K. Olson’s Major World Ecosystem Complexes Ranked by Carbon in Live
745 Vegetation: An Updated Database Using the GLC2000 Land Cover Product (NDP-017b).
746 <https://www.osti.gov/biblio/1389498>, 2006. **2006**.
- 747 (37) Yuan, H.; Dai, Y.; Xiao, Z.; Ji, D.; Shangguan, W. Reprocessing the MODIS Leaf Area
748 Index Products for Land Surface and Climate Modelling. *Remote Sens. Environ.* **2011**, *115*
749 (5), 1171–1187. <https://doi.org/10.1016/j.rse.2011.01.001>.
- 750 (38) Steenhuisen, F.; Wilson, S. J. Development and Application of an Updated Geospatial
751 Distribution Model for Gridding 2015 Global Mercury Emissions. *Atmos. Environ.* **2019**,
752 *211*, 138–150. <https://doi.org/10.1016/j.atmosenv.2019.05.003>.
- 753 (39) van der Werf, G. R.; Randerson, J. T.; Giglio, L.; van Leeuwen, T. T.; Chen, Y.; Rogers, B.
754 M.; Mu, M.; van Marle, M. J. E.; Morton, D. C.; Collatz, G. J.; Yokelson, R. J.; Kasibhatla,
755 P. S. Global Fire Emissions Estimates during 1997–2016. *Earth Syst. Sci. Data* **2017**, *9* (2),
756 697–720. <https://doi.org/10.5194/essd-9-697-2017>.
- 757 (40) Strobe, S. A.; Jaeglé, L.; Selin, N. E.; Jacob, D. J.; Park, R. J.; Yantosca, R. M.; Mason, R.
758 P.; Slemr, F. Air-Sea Exchange in the Global Mercury Cycle. *Global Biogeochem. Cycles*
759 **2007**, *21* (1), GB1017. <https://doi.org/10.1029/2006GB002766>.

- 760 (41) Khan, T. R.; Obrist, D.; Agnan, Y.; Selin, N. E.; Perlinger, J. A. Atmosphere-Terrestrial
761 Exchange of Gaseous Elemental Mercury: Parameterization Improvement through Direct
762 Comparison with Measured Ecosystem Fluxes. *Environ. Sci.: Processes Impacts* **2019**, *21*
763 (10), 1699–1712. <https://doi.org/10.1039/C9EM00341J>.
- 764 (42) Selin, N. E.; Jacob, D. J.; Yantosca, R. M.; Strode, S.; Jaeglé, L.; Sunderland, E. M. Global
765 3-D Land-Ocean-Atmosphere Model for Mercury: Present-Day versus Preindustrial Cycles
766 and Anthropogenic Enrichment Factors for Deposition. *Global Biogeochem. Cycles* **2008**,
767 *22* (2), GB2011. <https://doi.org/10.1029/2007GB003040>.
- 768 (43) Verstraete, M. M. Radiation Transfer in Plant Canopies: Transmission of Direct Solar
769 Radiation and the Role of Leaf Orientation. *J. Geophys. Res.* **1987**, *92* (D9), 10985.
770 <https://doi.org/10.1029/JD092iD09p10985>.
- 771 (44) Dinerstein, E.; Olson, D.; Joshi, A.; Vynne, C.; Burgess, N. D.; Wikramanayake, E.; Hahn,
772 N.; Palminteri, S.; Hedao, P.; Noss, R.; Hansen, M.; Locke, H.; Ellis, E. C.; Jones, B.;
773 Barber, C. V.; Hayes, R.; Kormos, C.; Martin, V.; Crist, E.; Sechrest, W.; Price, L.; Baillie,
774 J. E. M.; Weeden, D.; Suckling, K.; Davis, C.; Sizer, N.; Moore, R.; Thau, D.; Birch, T.;
775 Potapov, P.; Turubanova, S.; Tyukavina, A.; de Souza, N.; Pinteá, L.; Brito, J. C.;
776 Llewellyn, O. A.; Miller, A. G.; Patzelt, A.; Ghazanfar, S. A.; Timberlake, J.; Klöser, H.;
777 Shennan-Farpón, Y.; Kindt, R.; Lillesø, J.-P. B.; van Breugel, P.; Graudal, L.; Voge, M.;
778 Al-Shammari, K. F.; Saleem, M. An Ecoregion-Based Approach to Protecting Half the
779 Terrestrial Realm. *BioScience* **2017**, *67* (6), 534–545. <https://doi.org/10.1093/biosci/bix014>.
- 780 (45) Hurtt, G. C.; Chini, L.; Sahajpal, R.; Froking, S.; Bodirsky, B. L.; Calvin, K.; Doelman, J.
781 C.; Fisk, J.; Fujimori, S.; Klein Goldewijk, K.; Hasegawa, T.; Havlik, P.; Heinemann, A.;
782 Humpenöder, F.; Jungclaus, J.; Kaplan, J. O.; Kennedy, J.; Krisztin, T.; Lawrence, D.;
783 Lawrence, P.; Ma, L.; Mertz, O.; Pongratz, J.; Popp, A.; Poulter, B.; Riahi, K.; Shevliakova,
784 E.; Stehfest, E.; Thornton, P.; Tubiello, F. N.; van Vuuren, D. P.; Zhang, X. Harmonization
785 of Global Land Use Change and Management for the Period 850–2100 (LUH2) for CMIP6.
786 *Geosci. Model Dev.* **2020**, *13* (11), 5425–5464. <https://doi.org/10.5194/gmd-13-5425-2020>.
- 787 (46) Hosonuma, N.; Herold, M.; De Sy, V.; De Fries, R. S.; Brockhaus, M.; Verchot, L.;
788 Angelsen, A.; Romijn, E. An Assessment of Deforestation and Forest Degradation Drivers
789 in Developing Countries. *Environ. Res. Lett.* **2012**, *7* (4), 044009.
790 <https://doi.org/10.1088/1748-9326/7/4/044009>.
- 791 (47) Geist, H. J.; Lambin, E. F. Proximate Causes and Underlying Driving Forces of Tropical
792 Deforestation. *BioScience* **2002**, *52* (2), 143. [https://doi.org/10.1641/0006-3568\(2002\)052\[0143:PCAUDF\]2.0.CO;2](https://doi.org/10.1641/0006-3568(2002)052[0143:PCAUDF]2.0.CO;2).
- 794 (48) Gerson, J. R.; Szponar, N.; Zambrano, A. A.; Bergquist, B.; Broadbent, E.; Driscoll, C. T.;
795 Erkenwick, G.; Evers, D. C.; Fernandez, L. E.; Hsu-Kim, H.; Inga, G.; Lansdale, K. N.;
796 Marchese, M. J.; Martinez, A.; Moore, C.; Pan, W. K.; Purizaca, R. P.; Sánchez, V.; Silman,
797 M.; Ury, E. A.; Vega, C.; Watsa, M.; Bernhardt, E. S. Amazon Forests Capture High Levels
798 of Atmospheric Mercury Pollution from Artisanal Gold Mining. *Nat Commun* **2022**, *13* (1),
799 559. <https://doi.org/10.1038/s41467-022-27997-3>.
- 800 (49) Almeida, M. D.; Lacerda, L. D.; Bastos, W. R.; Herrmann, J. C. Mercury Loss from Soils
801 Following Conversion from Forest to Pasture in Rondônia, Western Amazon, Brazil.
802 *Environmental Pollution* **2005**, *137* (2), 179–186.
803 <https://doi.org/10.1016/j.envpol.2005.02.026>.
- 804 (50) Almeida, M. D.; Marins, R. V.; Paraquetti, H. H. M.; Bastos, W. R.; Lacerda, L. D.
805 Mercury Degassing from Forested and Open Field Soils in Rondônia, Western Amazon,
806 Brazil. *Chemosphere* **2009**, *77* (1), 60–66.
807 <https://doi.org/10.1016/j.chemosphere.2009.05.018>.

- 808 (51) Lacerda, L. D.; de Souza, M.; Ribeiro, M. G. The Effects of Land Use Change on Mercury
809 Distribution in Soils of Alta Floresta, Southern Amazon. *Environmental Pollution* **2004**,
810 *129* (2), 247–255. <https://doi.org/10.1016/j.envpol.2003.10.013>.
- 811 (52) Béliveau, A.; Lucotte, M.; Davidson, R.; do Canto Lopes, L. O.; Paquet, S. Early Hg
812 Mobility in Cultivated Tropical Soils One Year after Slash-and-Burn of the Primary Forest,
813 in the Brazilian Amazon. *Science of The Total Environment* **2009**, *407* (15), 4480–4489.
814 <https://doi.org/10.1016/j.scitotenv.2009.04.012>.
- 815 (53) Béliveau, A.; Lucotte, M.; Davidson, R.; Paquet, S.; Mertens, F.; Passos, C. J.; Romana, C.
816 A. Reduction of Soil Erosion and Mercury Losses in Agroforestry Systems Compared to
817 Forests and Cultivated Fields in the Brazilian Amazon. *Journal of Environmental*
818 *Management* **2017**, *203*, 522–532. <https://doi.org/10.1016/j.jenvman.2017.07.037>.
- 819 (54) Patry, C.; Davidson, R.; Lucotte, M.; Béliveau, A. Impact of Forested Fallows on Fertility
820 and Mercury Content in Soils of the Tapajós River Region, Brazilian Amazon. *Science of*
821 *The Total Environment* **2013**, *458–460*, 228–237.
822 <https://doi.org/10.1016/j.scitotenv.2013.04.037>.
- 823 (55) Comte, I.; Lucotte, M.; Davidson, R.; Reis de Carvalho, C. J.; de Assis Oliveira, F.;
824 Rousseau, G. X. Impacts of Land Uses on Mercury Retention in Long-Time Cultivated
825 Soils, Brazilian Amazon. *Water Air Soil Pollut* **2013**, *224* (4), 1515.
826 <https://doi.org/10.1007/s11270-013-1515-3>.
- 827 (56) Magarelli, G.; Fostier, A. Influence of Deforestation on the Mercury Air/Soil Exchange in
828 the Negro River Basin, Amazon. *Atmos. Environ.* **2005**, *39* (39), 7518–7528.
829 <https://doi.org/10.1016/j.atmosenv.2005.07.067>.
- 830 (57) Mainville, N.; Webb, J.; Lucotte, M.; Davidson, R.; Betancourt, O.; Cueva, E.; Mergler, D.
831 Decrease of Soil Fertility and Release of Mercury Following Deforestation in the Andean
832 Amazon, Napo River Valley, Ecuador. *Science of The Total Environment* **2006**, *368* (1),
833 88–98. <https://doi.org/10.1016/j.scitotenv.2005.09.064>.
- 834 (58) Roulet, M.; Lucotte, M.; Saint-Aubin, A.; Tran, S.; Rhéault, I.; Farella, N.; De Jesus Da
835 silva, E.; Dezencourt, J.; Sousa Passos, C.-J.; Santos Soares, G.; Guimarães, J.-R. D.;
836 Mergler, D.; Amorim, M. The Geochemistry of Mercury in Central Amazonian Soils
837 Developed on the Alter-Do-Chão Formation of the Lower Tapajós River Valley, Pará State,
838 Brazil. *Science of The Total Environment* **1998**, *223* (1), 1–24.
839 [https://doi.org/10.1016/S0048-9697\(98\)00265-4](https://doi.org/10.1016/S0048-9697(98)00265-4).
- 840 (59) Wasserman, J. C.; Campos, R. C.; Hacon, S. de S.; Farias, R. A.; Caires, S. M. Mercury in
841 Soils and Sediments from Gold Mining Liabilities in Southern Amazonia. *Quím. Nova*
842 **2007**, *30* (4). <https://doi.org/10.1590/S0100-40422007000400003>.
- 843 (60) Homann, P. S.; Darbyshire, R. L.; Bormann, B. T.; Morrissette, B. A. Forest Structure
844 Affects Soil Mercury Losses in the Presence and Absence of Wildfire. *Environ. Sci.*
845 *Technol.* **2015**, *49* (21), 12714–12722. <https://doi.org/10.1021/acs.est.5b03355>.
- 846 (61) Gamby, R. L.; Hammerschmidt, C. R.; Costello, D. M.; Lamborg, C. H.; Runkle, J. R.
847 Deforestation and Cultivation Mobilize Mercury from Topsoil. *Science of The Total*
848 *Environment* **2015**, *532*, 467–473. <https://doi.org/10.1016/j.scitotenv.2015.06.025>.
- 849 (62) Mazur, M.; Mitchell, C. P. J.; Eckley, C. S.; Eggert, S. L.; Kolka, R. K.; Sebestyen, S. D.;
850 Swain, E. B. Gaseous Mercury Fluxes from Forest Soils in Response to Forest Harvesting
851 Intensity: A Field Manipulation Experiment. *Science of The Total Environment* **2014**, *496*,
852 678–687. <https://doi.org/10.1016/j.scitotenv.2014.06.058>.
- 853 (63) Ma, M.; Wang, D.; Sun, R.; Shen, Y.; Huang, L. Gaseous Mercury Emissions from
854 Subtropical Forested and Open Field Soils in a National Nature Reserve, Southwest China.
855 *Atmospheric Environment* **2013**, *64*, 116–123.
856 <https://doi.org/10.1016/j.atmosenv.2012.09.038>.

- 857 (64) Eckley, C. S.; Eagles-Smith, C.; Tate, M. T.; Krabbenhoft, D. P. Surface-Air Mercury
858 Fluxes and a Watershed Mass Balance in Forested and Harvested Catchments.
859 *Environmental Pollution* **2021**, 277, 116869. <https://doi.org/10.1016/j.envpol.2021.116869>.
- 860 (65) Ramankutty, N.; Gibbs, H. K.; Achard, F.; Defries, R.; Foley, J. A.; Houghton, R. A.
861 Challenges to Estimating Carbon Emissions from Tropical Deforestation. *Global Change*
862 *Biol* **2007**, 13 (1), 51–66. <https://doi.org/10.1111/j.1365-2486.2006.01272.x>.
- 863 (66) Crespo-Lopez, M. E.; Augusto-Oliveira, M.; Lopes-Araújo, A.; Santos-Sacramento, L.;
864 Yuki Takeda, P.; Macchi, B. de M.; do Nascimento, J. L. M.; Maia, C. S. F.; Lima, R. R.;
865 Arrifano, G. P. Mercury: What Can We Learn from the Amazon? *Environment*
866 *International* **2021**, 146, 106223. <https://doi.org/10.1016/j.envint.2020.106223>.
- 867 (67) Michelazzo, P. A. M.; Fostier, A. H.; Magarelli, G.; Santos, J. C.; de Carvalho, J. A.
868 Mercury Emissions from Forest Burning in Southern Amazon. *Geophys. Res. Lett.* **2010**, 37
869 (9), L09809. <https://doi.org/10.1029/2009GL042220>.
- 870 (68) Lovejoy, T. E.; Nobre, C. Amazon Tipping Point. *Sci. Adv.* **2018**, 4 (2), eaat2340.
- 871 (69) Alves de Oliveira, B. F.; Bottino, M. J.; Nobre, P.; Nobre, C. A. Deforestation and Climate
872 Change Are Projected to Increase Heat Stress Risk in the Brazilian Amazon. *Commun.*
873 *Earth Environ.* **2021**, 2 (1), 207. <https://doi.org/10.1038/s43247-021-00275-8>.
- 874 (70) Griscom, B. W.; Adams, J.; Ellis, P. W.; Houghton, R. A.; Lomax, G.; Miteva, D. A.;
875 Schlesinger, W. H.; Shoch, D.; Siikamäki, J. V.; Smith, P.; Woodbury, P.; Zganjar, C.;
876 Blackman, A.; Campari, J.; Conant, R. T.; Delgado, C.; Elias, P.; Gopalakrishna, T.;
877 Hamsik, M. R.; Herrero, M.; Kiesecker, J.; Landis, E.; Laestadius, L.; Leavitt, S. M.;
878 Minnemeyer, S.; Polasky, S.; Potapov, P.; Putz, F. E.; Sanderman, J.; Silvius, M.;
879 Wollenberg, E.; Fargione, J. *Global Reforestation Potential Map*; Zenodo, 2017.
880 <https://doi.org/10.5281/zenodo.883444>.
- 881 (71) McKay, M. D.; Beckman, R. J.; Conover, W. J. Comparison of Three Methods for Selecting
882 Values of Input Variables in the Analysis of Output from a Computer Code. *Technometrics*
883 **1979**, 21 (2), 239–245. <https://doi.org/10.1080/00401706.1979.10489755>.
- 884 (72) Pacyna, J. M.; Travníkov, O.; De Simone, F.; Hedgecock, I. M.; Sundseth, K.; Pacyna, E.
885 G.; Steenhuisen, F.; Pirrone, N.; Munthe, J.; Kindbom, K. Current and Future Levels of
886 Mercury Atmospheric Pollution on a Global Scale. *Atmos. Chem. Phys.* **2016**, 16 (19),
887 12495–12511. <https://doi.org/10.5194/acp-16-12495-2016>.
- 888 (73) Fisher, J. A.; Schneider, L.; Fostier, A.-H.; Guerrero, S.; Guimarães, J. R. D.; Labuschagne,
889 C.; Leaner, J. J.; Martin, L. G.; Mason, R. P.; Somerset, V.; Walters, C. A Synthesis of
890 Mercury Research in the Southern Hemisphere, Part 2: Anthropogenic Perturbations. *Ambio*
891 **2023**, 52 (5), 918–937. <https://doi.org/10.1007/s13280-023-01840-5>.
- 892 (74) Zhang, Y.; Jacob, D. J.; Horowitz, H. M.; Chen, L.; Amos, H. M.; Krabbenhoft, D. P.;
893 Slemr, F.; St. Louis, V. L.; Sunderland, E. M. Observed Decrease in Atmospheric Mercury
894 Explained by Global Decline in Anthropogenic Emissions. *Proc. Natl. Acad. Sci. U.S.A.*
895 **2016**, 113 (3), 526–531. <https://doi.org/10.1073/pnas.1516312113>.
- 896 (75) Schartup, A. T.; Thackray, C. P.; Qureshi, A.; Dassuncao, C.; Gillespie, K.; Hanke, A.;
897 Sunderland, E. M. Climate Change and Overfishing Increase Neurotoxicant in Marine
898 Predators. *Nature* **2019**, 572 (7771), 648–650. <https://doi.org/10.1038/s41586-019-1468-9>.
- 899 (76) Zhang, Y.; Soerensen, A. L.; Schartup, A. T.; Sunderland, E. M. A Global Model for
900 Methylmercury Formation and Uptake at the Base of Marine Food Webs. *Global*
901 *Biogeochem. Cycles* **2020**, 34 (2). <https://doi.org/10.1029/2019GB006348>.
- 902 (77) Roulet, M.; Guimarães, J.R.D.; Lucotte, M. Methylmercury Production and Accumulation in
903 Sediments and Soils of an Amazonian Floodplain – Effect of Seasonal Inundation. *Water,*
904 *Air, and Soil Pollution* **2001**, 128, 41–60.

- 905 (78) Borrelli, P.; Robinson, D. A.; Panagos, P.; Lugato, E.; Yang, J. E.; Alewell, C.; Wuepper,
906 D.; Montanarella, L.; Ballabio, C. Land Use and Climate Change Impacts on Global Soil
907 Erosion by Water (2015–2070). *Proc. Natl. Acad. Sci. U.S.A.* **2020**, *117* (36), 21994–22001.
908 <https://doi.org/10.1073/pnas.2001403117>.
- 909 (79) Borrelli, P.; Robinson, D. A.; Fleischer, L. R.; Lugato, E.; Ballabio, C.; Alewell, C.;
910 Meusburger, K.; Modugno, S.; Schütt, B.; Ferro, V.; Bagarello, V.; Oost, K. V.;
911 Montanarella, L.; Panagos, P. An Assessment of the Global Impact of 21st Century Land
912 Use Change on Soil Erosion. *Nat Commun* **2017**, *8* (1), 2013.
913 <https://doi.org/10.1038/s41467-017-02142-7>.
- 914 (80) Bastin, J.-F.; Finegold, Y.; Garcia, C.; Mollicone, D.; Rezende, M.; Routh, D.; Zohner, C.
915 M.; Crowther, T. W. The Global Tree Restoration Potential. *Science* **2019**, *365* (6448), 76–
916 79. <https://doi.org/10.1126/science.aax0848>.
- 917 (81) Briggs, C.; Gustin, M. S. Building upon the Conceptual Model for Soil Mercury Flux:
918 Evidence of a Link Between Moisture Evaporation and Hg Evasion. *Water Air Soil Pollut*
919 **2013**, *224* (10), 1744. <https://doi.org/10.1007/s11270-013-1744-5>.
- 920 (82) Osterwalder, S.; Huang, J.-H.; Shetaya, W. H.; Agnan, Y.; Frossard, A.; Frey, B.; Alewell,
921 C.; Kretzschmar, R.; Biester, H.; Obrist, D. Mercury Emission from Industrially
922 Contaminated Soils in Relation to Chemical, Microbial, and Meteorological Factors.
923 *Environmental Pollution* **2019**, *250*, 944–952. <https://doi.org/10.1016/j.envpol.2019.03.093>.
- 924 (83) Agnan, Y.; Le Dantec, T.; Moore, C. W.; Edwards, G. C.; Obrist, D. New Constraints on
925 Terrestrial Surface–Atmosphere Fluxes of Gaseous Elemental Mercury Using a Global
926 Database. *Environ. Sci. Technol.* **2016**, *50* (2), 507–524.
927 <https://doi.org/10.1021/acs.est.5b04013>.
- 928 (84) Yuan, T.; Zhang, P.; Song, Z.; Huang, S.; Wang, X.; Zhang, Y. Buffering Effect of Global
929 Vegetation on the Air–Land Exchange of Mercury: Insights from a Novel Terrestrial
930 Mercury Model Based on CESM2-CLM5. *Environment International* **2023**, *174*, 107904.
931 <https://doi.org/10.1016/j.envint.2023.107904>.
- 932 (85) Liu, K.; Wu, Q.; Wang, L.; Wang, S.; Liu, T.; Ding, D.; Tang, Y.; Li, G.; Tian, H.; Duan,
933 L.; Wang, X.; Fu, X.; Feng, X.; Hao, J. Measure-Specific Effectiveness of Air Pollution
934 Control on China’s Atmospheric Mercury Concentration and Deposition during 2013–2017.
935 *Environ. Sci. Technol.* **2019**, *53* (15), 8938–8946. <https://doi.org/10.1021/acs.est.9b02428>.
- 936 (86) EPA. *National Emission Standards for Hazardous Air Pollutants: Coal- and Oil-Fired*
937 *Electric Utility Steam Generating Units—Reconsideration of Supplemental Finding and*
938 *Residual Risk and Technology Review*; EPA–HQ–OAR–2018–0794; FRL–9988–93–OAR;
939 2019; pp 2670–2704. <https://www.govinfo.gov/content/pkg/FR-2019-02-07/pdf/2019-00936.pdf>.
- 941 (87) Environment and Climate Change Canada. *Evaluation of the Effectiveness of Risk*
942 *Management Measures for Mercury*; En14-411/2020E-PDF; 2020; pp 1–43.
943 <https://www.canada.ca/en/environment-climate-change/services/management-toxic-substances/evaluation-effectiveness-risk-management-measures-mercury.html>.
- 944 (88) Bruno, D. E.; De Simone, F.; Cinnirella, S.; Hedgecock, I. M.; D’Amore, F.; Pirrone, N.
945 Reducing Mercury Emission Uncertainty from Artisanal and Small-Scale Gold Mining
946 Using Bootstrap Confidence Intervals: An Assessment of Emission Reduction Scenarios.
947 *Atmosphere* **2022**, *14* (1), 62. <https://doi.org/10.3390/atmos14010062>.
- 948 (89) Mulvaney, K. M.; Selin, N. E.; Giang, A.; Muntean, M.; Li, C.-T.; Zhang, D.; Angot, H.;
949 Thackray, C. P.; Karplus, V. J. Mercury Benefits of Climate Policy in China: Addressing
950 the Paris Agreement and the Minamata Convention Simultaneously. *Environ. Sci. Technol.*
951 **2020**, *54* (3), 1326–1335. <https://doi.org/10.1021/acs.est.9b06741>.
- 952

- 953 (90) Rafaj, P.; Cofala, J.; Kuenen, J.; Wyrwa, A.; Zyśk, J. Benefits of European Climate Policies
954 for Mercury Air Pollution. *Atmosphere* **2014**, *5* (1), 45–59.
955 <https://doi.org/10.3390/atmos5010045>.
- 956 (91) Wohlgemuth, L.; Rautio, P.; Ahrends, B.; Russ, A.; Vesterdal, L.; Waldner, P.;
957 Timmermann, V.; Eickenscheidt, N.; Fürst, A.; Greve, M.; Roskams, P.; Thimonier, A.;
958 Nicolas, M.; Kowalska, A.; Ingerslev, M.; Merilä, P.; Benham, S.; Iacoban, C.; Hoch, G.;
959 Alewell, C.; Jiskra, M. Physiological and Climate Controls on Foliar Mercury Uptake by
960 European Tree Species. *Biogeosciences* **2022**, *19* (5), 1335–1353.
961 <https://doi.org/10.5194/bg-19-1335-2022>.
- 962 (92) COP26. *Glasgow Leaders' Declaration on Forests and Land Use*; 2021.
963 <https://ukcop26.org/glasgow-leaders-declaration-on-forests-and-land-use/>.

1 **Supplementary Information (SI) for**

2 **Deforestation as an anthropogenic driver of mercury pollution**

3
4 *Aryeh Feinberg^{a*}, Martin Jiskra^{b*}, Pasquale Borrelli^c, Jagannath Biswakarma^{b,d}, and Noelle*
5 *E. Selin^{a,e}*

6 ^a Institute for Data, Systems, and Society, Massachusetts Institute of Technology, Cambridge,
7 MA 02139, USA

8 ^b Environmental Geosciences, University of Basel, Basel 4056, Switzerland

9 ^c Department of Science, Roma Tre University, Rome 00146, Italy

10 ^d Department of Water Resources and Drinking Water, Eawag, Dübendorf 8600, Switzerland

11 ^e Department of Earth, Atmospheric, and Planetary Sciences, Massachusetts Institute of
12 Technology, Cambridge, MA 02139, USA

13 *Correspondence to: arifeinberg@gmail.com (A.F.); martin.jiskra@gmail.com (M.J.)

14
15 Number of pages: 19

16 Number of figures: 11

17 Number of tables: 6

18

19 **Section S1. Soil emissions parameterization**

20 We improved the model's parametrization of Hg^0 soil emissions by adopting a new formulation for the
 21 parametrization, suggested by Khan et al.¹:

$$22 \quad E_{\text{soil}} = aC^bR_g^c \quad (\text{Eq. S1})$$

23 where E_{soil} are soil emissions ($\text{ng m}^{-2}\text{h}^{-1}$), C is the concentration of Hg in soils ($\mu\text{g g}^{-1}$), R_g is the solar
 24 radiation flux at the ground (W m^{-2}), and a , b , and c are coefficients.

25
 26 As in Selin et al.², the solar radiation at ground (R_g) is determined by considering attenuation of the
 27 solar radiation flux (R_s) by shading from the overhead canopy, parametrized by the leaf area index
 28 (LAI):

$$29 \quad R_g = R_s \exp\left(-\frac{\alpha\text{LAI}}{\cos\theta}\right) \quad (\text{Eq. S2})$$

30 where $\alpha = 0.5$, assuming extinction from a random angular distribution of leaves³ and θ is the solar
 31 zenith angle.

32
 33 We compiled several relevant observational constraints for the parametrization in Tables S1 and S2.
 34 Observational studies from the Amazon region suggest that deforestation has a large impact on soil
 35 emissions due to removal of canopy shading, showing factors of 1.8×, 6.7×, and >31× more emissions
 36 in forested compared to deforested land plots (Table S1). Observational studies from other regions
 37 find a similarly high sensitivity of soil emissions to the presence of forest: open fields in China
 38 showed 6–10 times higher Hg emissions than forests⁴ and logging in the US flipped the surface-air
 39 Hg^0 flux from net deposition to net emissions ($-2.2 \mu\text{g m}^{-2}\text{yr}^{-1}$ to $+5.5 \mu\text{g m}^{-2}\text{yr}^{-1}$)⁵. For extratropical
 40 grassland soil emissions, we use the compiled median values from Zhu et al.⁶ and Agnan et al.⁷

41
 42 We conducted a parameter sweep of a , b , and c , calculating globally-gridded soil emissions using
 43 annual solar radiation data (Fig. S1). Sensitivity simulations showed that the ratio of deforested to
 44 forested soil emissions in the Amazon (median value 6.7) can tune the exponent for the radiation term
 45 (c in Eq. S1), i.e., the response of emissions to canopy shading. The exponent for the soil
 46 concentration term (b) was tuned with the ratio of deforested Amazon soil emissions (Table S1) to
 47 extratropical grassland soil emissions from the Northern Hemisphere from two review studies^{6,7}
 48 (overall Amazon to extratropical ratio of 5.3). Lastly, after these coefficients are tuned, the prefactor a
 49 is adjusted so that predicted annual mean emissions match the observed median magnitudes of
 50 Amazon deforested soil emissions ($23 \mu\text{g m}^{-2}\text{yr}^{-1}$) and extratropical grassland emissions ($4.3 \mu\text{g m}^{-2}$
 51 yr^{-1}).

52
 53 We recognize the uncertainties in the observed data used to tune this parametrization, and thus we
 54 constructed 100 alternative parametrizations that fit within observed data bounds (Table S5). These
 55 parametrizations were applied in offline uncertainty analyses to assess 95% confidence intervals in the
 56 fluxes driven by deforestation (Section S4).

57
 58

59 **Table S1.** Literature review of available Hg⁰ soil emission flux measurements from the Amazon
 60 region, differentiated by land cover type.

Reference	Location	Site	Deforested Hg ⁰ flux ($\mu\text{g m}^{-2} \text{yr}^{-1}$)	Forested Hg ⁰ flux ($\mu\text{g m}^{-2} \text{yr}^{-1}$)	Flux ratio (deforest:forest)
Magarelli and Fostier ⁸	Negro River Basin, Brazil	#1	27 ± 9	0.6 ± 1.5	
		#2	19	-1.0 ± 0.8	
		#3	9.8 ± 0.7		
		Mean	18	-0.2	> 31 ^a
Almeida et al. ⁹	Rondônia, Brazil	#1	79 ± 110	44 ± 18	1.8
Carpi et al. ¹⁰	Acre, Brazil	#1	19 ± 2	2.9 ± 0.8	6.7
		#2	230 ^b		
Median			23	1.8	6.7

61 ^alower limit calculated assuming the forested flux is equal to site #1, as site #2 shows negative overall flux;
 62 deforested flux assumed as mean.

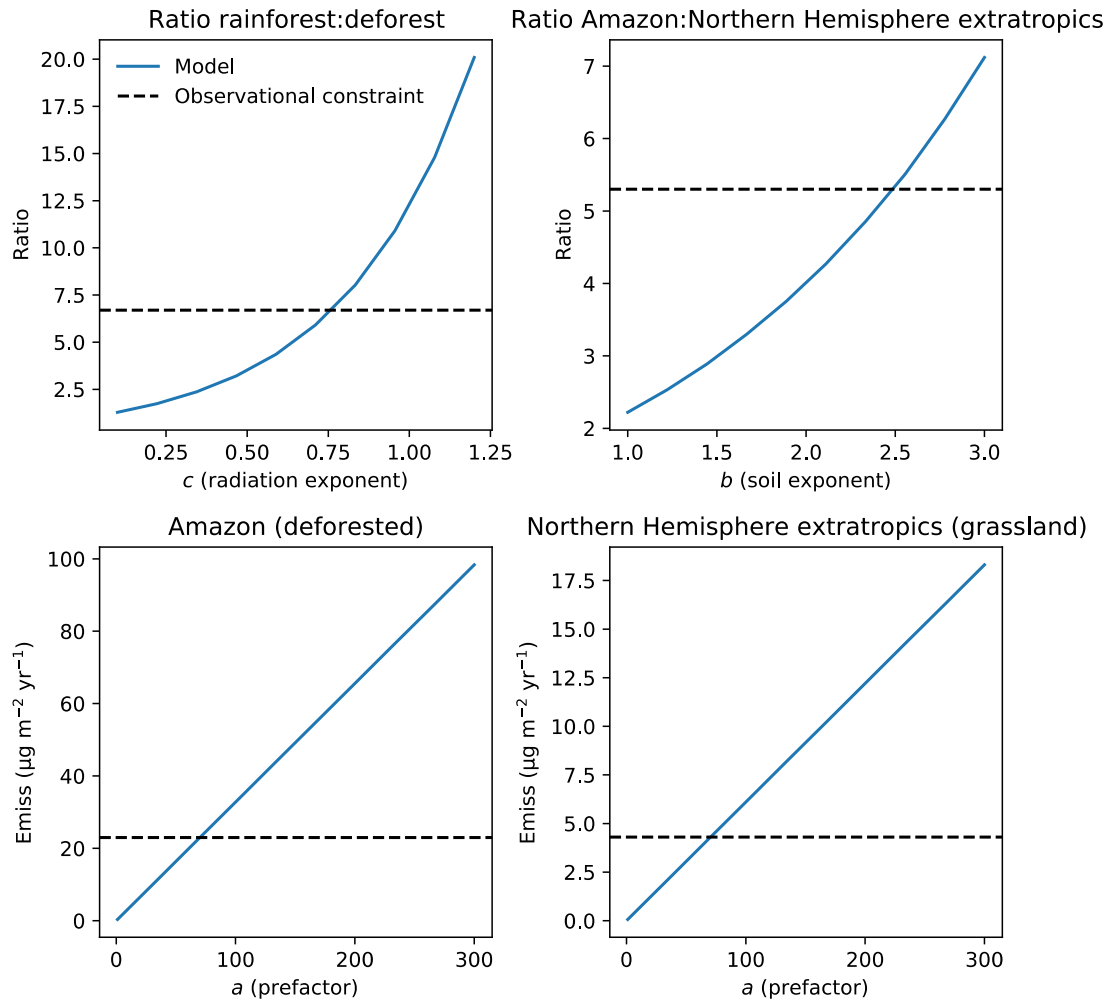
63 ^bthis site was 2-months post-fire and soil temperatures were still elevated; this flux is excluded from ratio
 64 calculations

65

66 **Table S2.** Observational constraints used to tune the soil emissions parametrization.

Constraint	Value	Reference	Coefficient constrained
Amazon deforested soil emissions ($\mu\text{g m}^{-2} \text{yr}^{-1}$)	23	Table S1	<i>a</i>
Extratropical grassland soil emissions ($\mu\text{g m}^{-2} \text{yr}^{-1}$)	4.3 [†]	Zhu et al. ⁶ ; Agnan et al. ⁷	<i>a</i>
Ratio of Amazon to extratropical soil emissions	5.3	(23:4.3)	<i>b</i>
Ratio of deforested to forested Amazon soil emissions	6.7	Table S1	<i>c</i>

67 [†]average of grassland median Hg⁰ fluxes from the two independent review studies



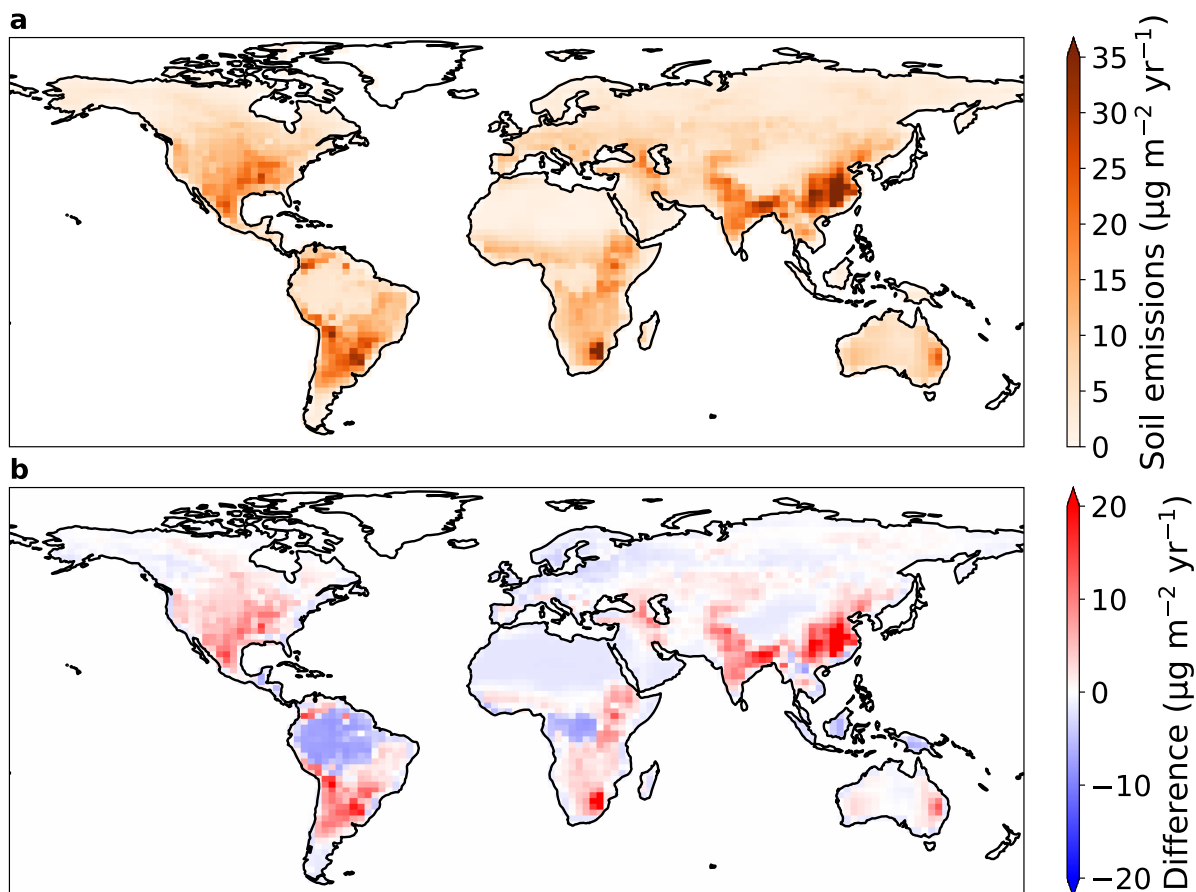
68

69 **Figure S1.** Parameter tuning (Eq. S1) to match observational constraints from Table S2.

70

71 The tuning procedure is illustrated in Fig. S1, yielding best matches for $a = 71$, $b = 2.5$, and
 72 $c = 0.76$. We compare the gridded annual mean soil emissions from the previous soil emission
 73 parametrization (GEOS-Chem v12.8) and the current study (Eq. S1) in Fig. S2. Global annual mean
 74 soil Hg^0 emissions in the new parametrizations (954 Mg yr^{-1}) is similar to the predictions from two
 75 GEOS-Chem studies^{11,12} using the previous parametrization: $860 \pm 440 \text{ Mg yr}^{-1}$ and 910 Mg yr^{-1} . The
 76 spatial distribution of emissions (Fig. S2) shows a decrease in vegetated regions (e.g., the Amazon and
 77 Congo rainforests) and an increase in regions with high soil Hg concentrations (e.g., eastern China).

78



79
 80 **Figure S2.** (a) Annual mean soil emissions of Hg⁰ with the new parametrization. (b) Difference
 81 between new and old (GEOS-Chem v12.8) soil emissions parametrizations (new minus old).
 82

83 **Section S2. Observational constraints on deforestation Hg fluxes**

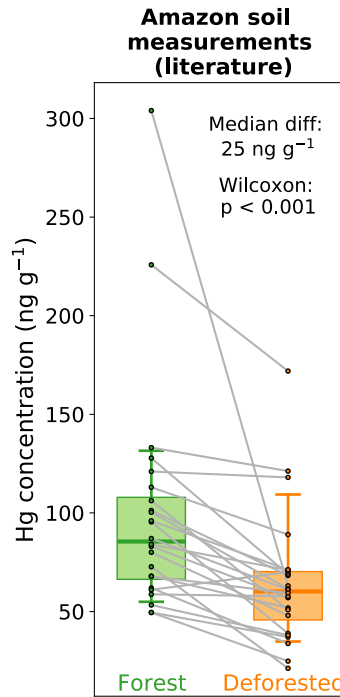
84 There are several available sources of information that can be used to validate the deforestation
 85 emission factors (EF) calculated by GEOS-Chem (Fig. 1, SI Spreadsheet):
 86

87 1) *Soil Hg concentration measurements of paired forest-deforested sites:*

88 Previous studies have measured the concentrations of Hg soils at deforested sites (C_d) and nearby
 89 forest (C_f) plots. For this analysis, we assume that the difference in these soil concentrations is due to
 90 mainly the change in atmospheric exchange, which is supported by the magnitude of modeled erosion
 91 fluxes (Section S6) and available measurements⁵. We use the following equation to convert the
 92 difference in these concentrations to a deforestation emission factor of Hg in Mg m⁻² yr⁻¹:

93
$$\text{Total EF} = \frac{(C_d - C_f) \times \rho \times h}{t_d} \quad (\text{S3})$$

94 where ρ is the density of the soil, h is the depth of the soil layer, and t_d is the time since deforestation.
 95 In the US (Nearctic), there have been studies in Ohio¹³ and Oregon¹⁴ with measurements of Hg in
 96 deforested and forested soils, which we use to calculate deforestation EFs for the Nearctic. For the
 97 Amazon, more measurements are available (24 pairs of soil plots)^{8-10,15-25}. We compiled a literature
 98 database of studies that compared Hg concentrations in deforested Amazonian soils with nearby forest
 99 plots (Fig. S3; SI Spreadsheet). Deforested sites show a consistent decrease compared to paired
 100 forested sites (p -value < 0.001; Wilcoxon signed-rank test), with the median decrease being 25 ng g⁻¹
 101 (10th–90th percentile: 2–58 ng g⁻¹). To calculate a deforestation EF for the Amazon, we apply this
 102 concentration decrease in Eq. S3 and assume an average Amazon soil density of 1.25 ng g⁻¹, a surface
 103 soil layer of 10 cm, and that deforested soils in the literature studies were measured 10 years after
 104 deforestation.



105
 106 **Figure S3.** Measured Hg concentrations in forest (green) and deforested (orange) soils (0–20 cm
 107 depth) from the literature ($n = 24$)^{8–10,15–25}. Box plots show the median values (solid lines),
 108 interquartile range (shaded), and 10th and 90th percentiles (whiskers). Gray lines connect paired sites
 109 from the same study. Listed p -value (<0.001) refers to the Wilcoxon signed-rank test of the null
 110 hypothesis that paired forest and deforested sites come from the same distribution.

111
 112 2) *Terrestrial-atmosphere exchange models validated by Hg observations:*

113 An estimate for the deforestation EF over China is available from the Wang et al.²⁶ modeling study.
 114 We use their area-averaged mean fluxes over forest and agricultural land cover to calculate a
 115 deforestation emission factor:

116
$$\text{Total EF} = (E_d - D_d) - (E_f - D_f) \quad (\text{S4})$$

117 where E_d and E_f are the terrestrial emission fluxes ($\text{Mg m}^{-2} \text{yr}^{-1}$) from Chinese agricultural land and
 118 forest, and D_d and D_f are the deposition fluxes ($\text{Mg m}^{-2} \text{yr}^{-1}$) to Chinese agricultural land and forest.
 119 Although this EF estimate is model-based, the Wang et al.²⁶ model was validated extensively with
 120 available terrestrial-atmosphere exchange measurements from China.

121
 122 3) *Dynamic flux chamber measurements of forested and deforested soils:*

123 Additional studies investigating the impact of deforestation on atmospheric fluxes quantified the
 124 response of soil emissions using dynamic flux chamber measurements^{5,8–10,27,28}. We compare these
 125 measurements to the soil-only EF modeled by GEOS-Chem. The soil emission factors measured by
 126 the studies is calculated as the difference between soil emissions ($\text{Mg m}^{-2} \text{yr}^{-1}$) over deforested and
 127 forested soils:

128
$$\text{Soil EF} = E_d - E_f \quad (\text{S5})$$

129
 130 The comparison between GEOS-Chem simulated deforestation EFs and observation-derived values is
 131 summarized in Fig. 1. Observations are only available from three regions (Amazon, China and
 132 Nearctic). We found further references investigating the impact of deforestation on Hg for the
 133 Palearctic region^{29,30}, yet these focused on measuring Hg concentrations in aquatic media and
 134 methylation potential rather than soil concentrations or atmospheric exchange. Australian soil
 135 measurements^{31,32} have been made before and after vegetation burning events, but do not cover the
 136 longer term soil Hg response to deforestation.

137
 138 The modeled EF estimates and their uncertainties overlap with observation-derived EFs for all 3
 139 regions. If anything, the modeled best estimate used in online simulations is conservative compared to

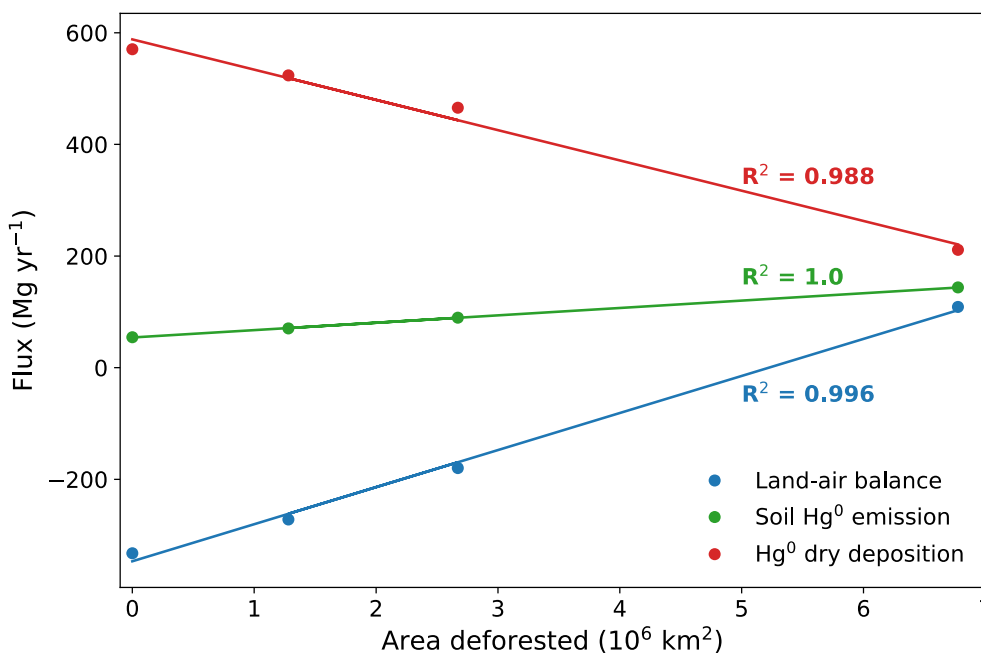
140 available observations, showing generally lower EFs (Fig. 1). However, it is unclear whether the
 141 sparse observations available are representative of the overall region. The modeled EF uncertainty
 142 estimates cover 1–2 orders of magnitude, emphasizing the current uncertainties in the response of Hg
 143 fluxes to deforestation. Figure 1 also reveals the regions where no observations of the impact of
 144 deforestation on Hg cycling are currently available. Specifically, the Afrotropic and Indomalayan
 145 domains would be priorities for future measurement campaigns, given the current impact of
 146 deforestation in those regions (Fig. 2). It remains unknown whether Southeast Asian and African
 147 rainforests show similarly high levels of Hg in litterfall as the Amazon rainforest³³.

148

149 Section S3. Global deforestation-driven emissions estimates

150 We use perturbation simulations in which a set area within each region is deforested to calculate each
 151 deforestation EF. In the EF approach, we assume that 1) land-air fluxes respond linearly to deforested
 152 area and 2) spatial variability in the deforestation response within regions can be ignored. We explored
 153 the validity these assumptions using the four Amazon deforestation scenario simulations conducted in
 154 this work (Fig. S4). In the Amazon simulations — the reference simulation with 2003 forest cover
 155 (HIST), governance scenario for 2050 (GOV), business-as-usual for 2050 (BAU), and savannization
 156 (SAV) — different areas (both in spatial pattern and extent) were deforested in the Amazon region.
 157 The total fluxes from the Amazon basin for Hg⁰ dry deposition, soil Hg⁰ emissions, and the overall
 158 land-air balance of Hg all respond linearly ($R^2 > 0.98$) to the magnitude of the deforested area.
 159 Therefore, the approach of calculating deforestation EFs and scaling these with deforested areas would
 160 likely not be highly sensitive to the spatial distribution and amount of deforestation. Therefore, we
 161 conducted 7 other idealized deforestation simulations for the other land regions (Fig. S5).

162



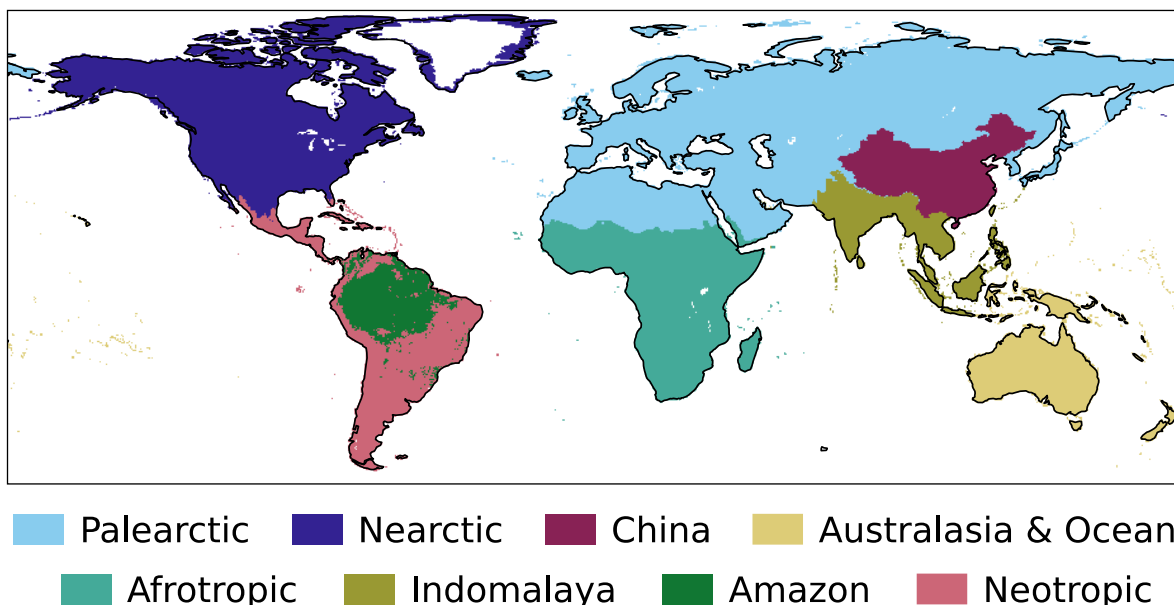
163

164 **Figure S4.** Relationship between land-air fluxes and the area deforested in GEOS-Chem simulations
 165 for the Amazon rainforest. Fluxes are averaged over the Amazon rainforest domain and listed R^2
 166 values refer to linear models.

167

168 Additional data related to the calculation of historical deforestation-driven emissions of Hg are
 169 presented in this section. The maps defining the regions used in this study is shown in Fig. S5. Table
 170 S3 tabulates the results from the perturbation simulations for the different regions and the resultant
 171 emission factors. Fig. S6 explores the impact of choosing different time horizons for the deforestation
 172 area on the calculated Hg emissions globally and by country. Fig. S7 shows the map of Hg
 173 deforestation-driven emissions, assuming a 45 year time horizon (deforestation area of 1970–2014
 174 from the LUH2 dataset³⁴).

175



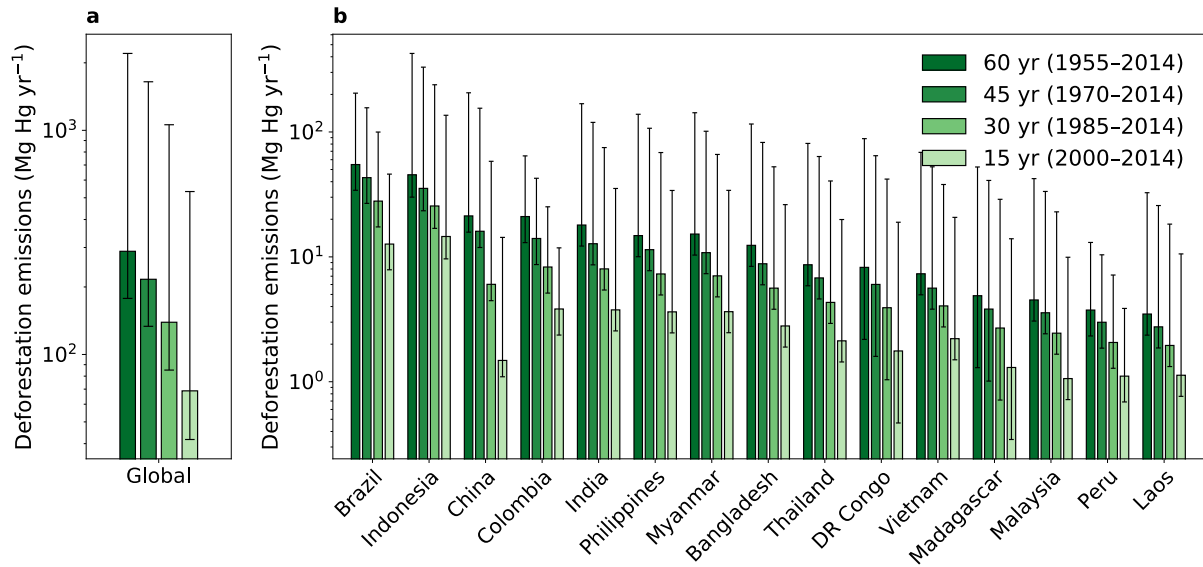
176
177
178
179
180

Figure S5. Definition of regions used to calculate the deforestation emission factors.

181 **Table S3.** Results from the deforestation perturbation simulations in GEOS-Chem for determining the
182 response of land-air fluxes to deforesting a specified area. Emissions factors are listed with the 95%
183 confidence interval calculated in offline simulations assessing the uncertainties due to model
184 parameters (Section S4).

Realm	Area deforested (km ²)	Change in emissions (Mg yr ⁻¹)	Change in deposition (Mg yr ⁻¹)	Change in net emissions (Mg yr ⁻¹)	Emissions factor (Mg m ⁻² yr ⁻¹) [95% confidence interval]
Afrotropic	3 644 969	29.1	-10.0	39.1	1.1×10^{-5} [2.8×10^{-6} to 1.2×10^{-4}]
Neotropic	2 422 577	13.0	-4.9	17.9	7.4×10^{-6} [4.8×10^{-6} to 5.7×10^{-5}]
Indomalaya	2 626 474	31.6	-28.3	59.9	2.3×10^{-5} [1.5×10^{-5} to 2.1×10^{-4}]
Palearctic	4 221 663	5.8	-4.3	10.1	2.4×10^{-6} [7.6×10^{-8} to 2.3×10^{-5}]
Nearctic	4 606 898	31.6	-17.4	48.9	1.1×10^{-5} [7.1×10^{-6} to 6.2×10^{-5}]
Australasia	1 088 250	1.9	-4.8	6.6	6.1×10^{-6} [8.3×10^{-7} to 5.4×10^{-5}]
China	1 141 180	16.6	-10.1	26.7	2.3×10^{-5} [1.7×10^{-5} to 2.3×10^{-4}]
Amazon	6 775 429	96.2	-394.0	490.2	7.2×10^{-5} [4.5×10^{-5} to 2.0×10^{-4}]

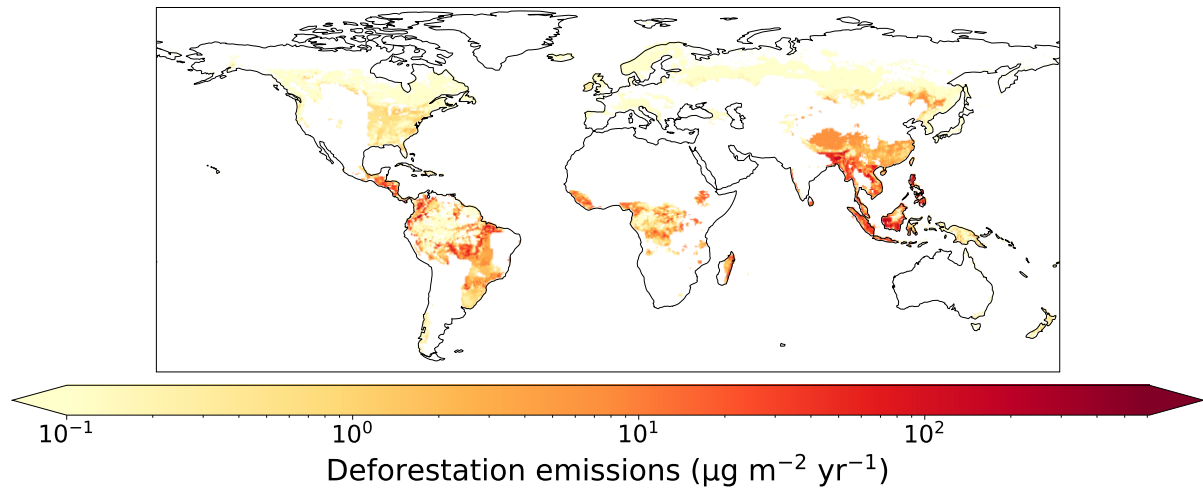
185



186

187 **Figure S6.** (a) Global and (b) country-level deforestation emissions of Hg for the top 15 emitting
 188 countries. Results are summarized accumulating deforested area over different time horizons (15
 189 years, 30 years, 45 years, and 60 years) before 2015. Error bars refer to the 95% confidence interval
 190 based on the uncertainty in model parameters (Section S4).

191



192

193 **Figure S7.** Map of net emissions of Hg from deforestation calculated over a 45 year time horizon
 194 before 2015 (1970–2014), using deforested area from the LUH2 dataset³⁴.

195

196

197 **Section S4. Model uncertainty analysis**

198

199 **Table S4.** Parameter uncertainty bounds applied in the uncertainty analysis.

Parameter	Min	Max	Units	Distribution	Comment
Soil emission parametrization	1	100	-	Uniform	Integer representing one of 100 reasonable parametrizations calculated within the range of observed uncertainties (Table S5)
Percentile of replaced LAI when building scenarios	10	90	-	Uniform	e.g., deforested Amazon area is assigned 10 th percentile LAI of HIST savanna, instead of mean for default estimate
Dry deposition Hg ⁰ reactivity (f_0) Amazon rainforest	10 ⁻²	0.5	-	Loguniform	Based on Feinberg et al. ³³ , within range of available vegetation uptake measurements
Dry deposition Hg ⁰ reactivity (f_0) other rainforests	10 ⁻⁵	0.2	-	Loguniform	Based on Feinberg et al. ³³ ; no available measurements from other rainforests, leading to wider f_0 uncertainty
Dry deposition Hg ⁰ reactivity (f_0) elsewhere	10 ⁻⁵	5 × 10 ⁻⁵	-	Uniform	Based on Feinberg et al. ³³ , within range of available vegetation uptake measurements
Biomass burning emission factor for Amazon	350	615	µg m ⁻²	Uniform	Estimated range in literature ^{10,35,36}

200

201

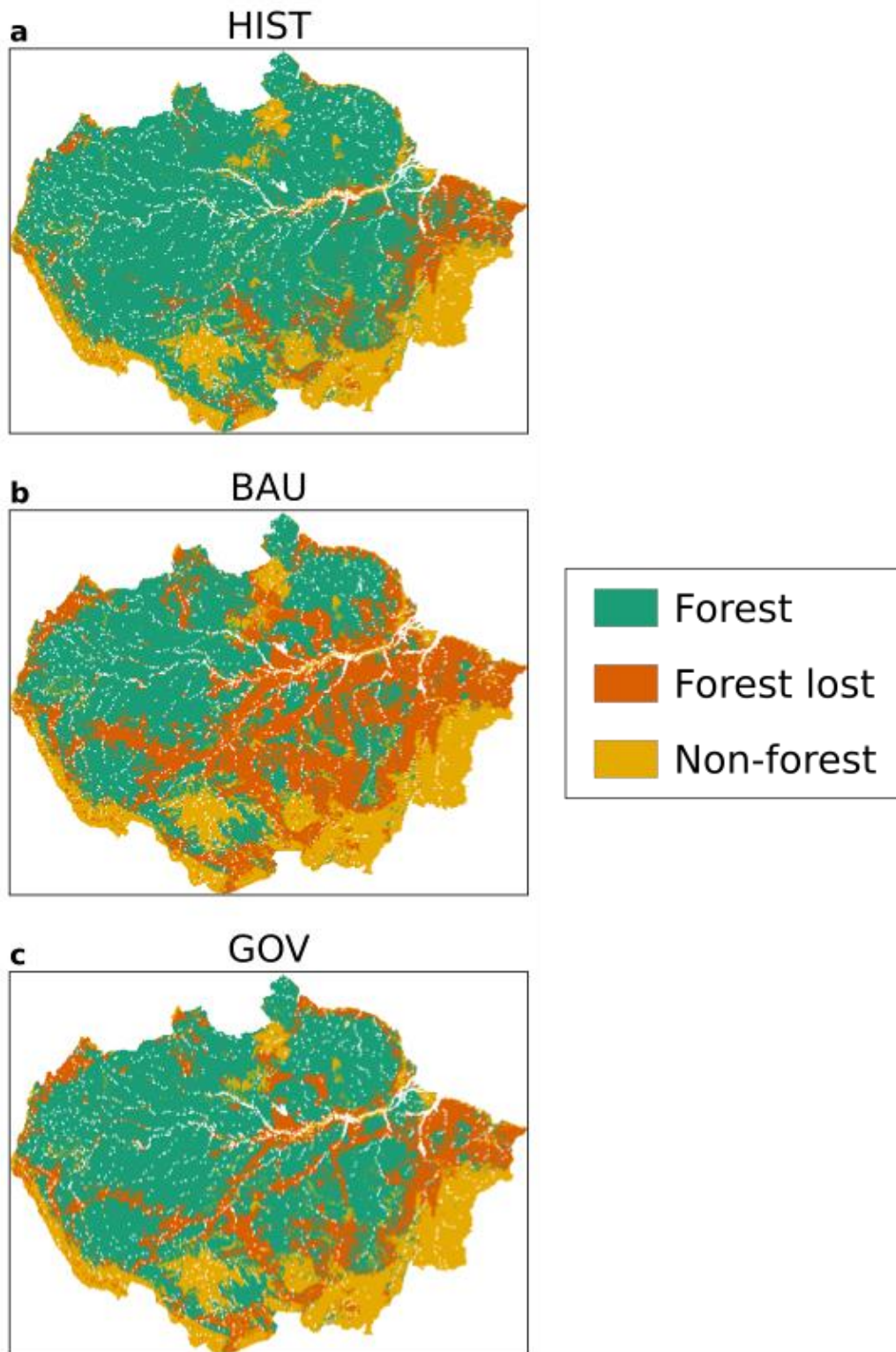
202 **Table S5.** Bounds of observed parameters used to calculate 100 reasonable soil emission
 203 parametrizations, which are then applied in the uncertainty analysis (Table S4).

Parameter	Min	Max	Units	Comment
Ratio of deforested to forested Amazon soil emissions	1.8	31	-	Range from Table S1
Ratio of Amazon to extratropical soil emissions	3.5	8	-	Assume 50% error from Table S2
Extratropical grassland soil emissions	3.5	11.4	µg m ⁻² yr ⁻¹	Grasslands and background soil range from literature reviews ^{6,7}
Deforested Amazon soil emissions	9.8	79	µg m ⁻² yr ⁻¹	Range from Table S1

204

205

206 **Section S5. Scenarios for Amazon deforestation and global reforestation**

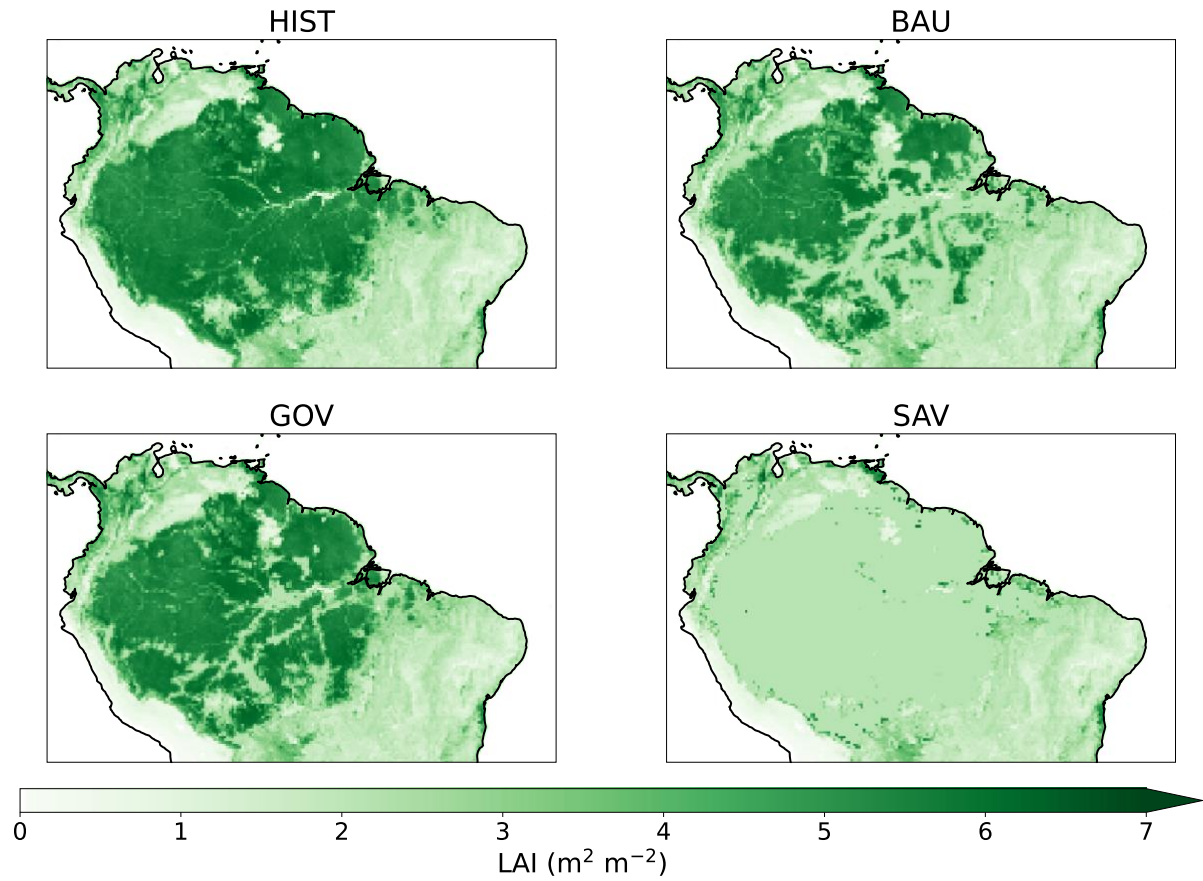


207

208 **Figure S8.** Map of the Amazon basin showing the area of forest, forest loss and rangeland and
209 agriculture in (a) HIST; and projections for 2050 in (b) Business as Usual (BAU) and (c) Governance
210 (GOV) scenarios (replotted from Soares-Filho et al.³⁷ data).

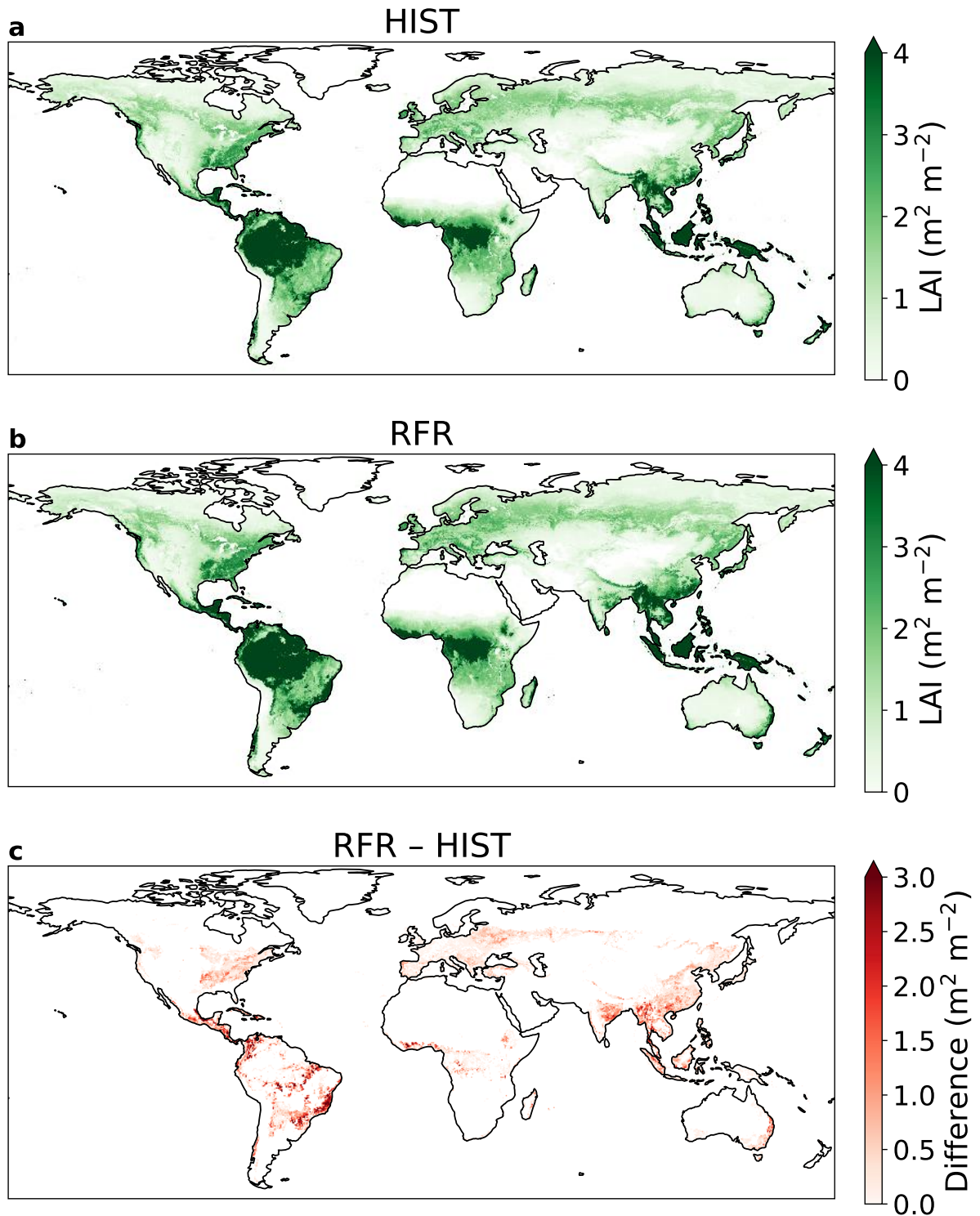
211

212



213

214 **Figure S9.** Annual mean leaf area index (LAI) maps for the Amazon deforestation scenarios at 0.25°
215 $\times 0.25^\circ$ resolution. The simulations names refer to the following scenarios: reference (HIST),
216 Business-as-usual (BAU), Governance (GOV), and Savannization (SAV).



217

218 **Figure S10.** Annual mean leaf area index (LAI) maps at $0.25 \times 0.25^\circ$ resolution for: (a) the reference
 219 (HIST) scenario (b) Reforestation scenario (RFR) (c) Difference between RFR and HIST.
 220

221 **Section S6. Impact of Amazon deforestation on erosion**

222 Previous field studies^{15,38} have suggested that erosion of Hg is increased after deforestation in the
 223 Amazon, measuring enhanced runoff of Hg in deforested catchments. We estimated the change in soil
 224 displacement by water erosion (soil erosion) in the Amazon deforestation scenarios using the RUSLE-
 225 based³⁹ modeling platform Global Soil Erosion Modeling (GloSEM)^{40,41}. As a detachment-limited soil
 226 erosion prediction model, GloSEM estimates soil erosion (expressed as a mass of soil lost per unit area
 227 and time, $\text{Mg ha}^{-1} \text{yr}^{-1}$) due to inter-rill and rill erosion processes by multiplication of six contributing

228 factors. The modeling scheme follows the same principle of most RUSLE-type models or more
 229 complex catchment-scale process-based models, with a driving force (erosivity of the climate, R), a
 230 resistance term (erodibility of the soil, K) and other factors representing the farming choice, i.e.,
 231 topographical conformation of the field (LS), cropping system (C), and soil conservation practices (P).
 232

233 Our approach for calculating soil erosion in the Amazon scenarios is similar to the GloSEM
 234 parametrization adopted by Borrelli et al.^{40,41} to estimate human-induced soil erosion change between
 235 2001 and 2070 at a global scale. The horizontal resolution of the native soil erosion modeling is 250 ×
 236 250 m. The calculation of erosivity (R), erodibility (K), topographical conformation of the field (LS),
 237 and soil conservation practices (P) factors are described in Borrelli et al.^{40,41}. We acknowledge that the
 238 calculation of erosion model factors for the Amazon rainforest may be associated with higher
 239 uncertainties than other regions due to the lower density in meteorological stations⁴² and soil sampling
 240 sites⁴³. For this study, we adapted the computation of the land cover and management factor (C-
 241 factor), which measures the combined effect of vegetation cover and cropping system variables on the
 242 soil erosion process. We parametrize the C-factor according to two layers of information: 1) the spatial
 243 dimension of land use classes according to the deforestation scenarios from Soares-Filho et al.³⁷
 244 (described below); 2) the vegetation condition in each land use class using the MODIS MOD44B
 245 Vegetation Continuous Fields product (VCF) (~250m spatial resolution) as a proxy to quantify (i)
 246 surface vegetation cover, (ii) tree cover, and (iii) bare soil. As we focus our analysis on comparing the
 247 forest coverage in the years 2003 and 2050, the baseline vegetation condition is given by the average
 248 VCF values over the years 2000, 2001 and 2002. The C-factor for noncropland areas (C_{nc}) is estimated
 249 in two steps. First, a preliminary C-factor (C_p) not considering tree cover is calculated as:

$$250 \quad C_p = C_{min} + ((C_{max} - C_{min}) NVS) \quad (S6)$$

251 where the C_{min} (0.01) and C_{max} (0.15) express the potential range in C-factor values for dense to
 252 sparse grassland cover. NVS (non-vegetated surface) is spatially defined using the MODIS MOD44B
 253 VCF data normalized to a range from 0 to 1 and describes the percentage of ground covered by any
 254 vegetation type. For the NVS, the C-factor is set to 0.5. Within the next step, the final land cover and
 255 management C-factor for non-croplands (C_{nc}) is computed including the tree coverage (TC) defined
 256 using the MODIS MOD44B VCF normalized to range from 0 to 1:

$$257 \quad C_{nc} = C_{p \ min} + ((C_{p \ max} - C_{p \ min}) TC) \quad (S7)$$

258 where the $C_{p \ min}$ and $C_{p \ max}$ values are set to 0.0001 (100% canopy cover) and 0.009 (sparse forest
 259 vegetation).
 260

261 While the deforestation scenarios proposed by Soares-Filho et al.³⁷ provide a spatial quantification of
 262 the forest losses between 2003 and 2050, the annual shares of conversion from forest to grassland or
 263 cropland are separate from the annual projection of the Land-Use Harmonization (LUH2) data³⁴,
 264 which provides fractional land-use patterns (850-2100) at $0.25^\circ \times 0.25^\circ$ resolution. The downscaling
 265 of the LUH2 fractional cropland and grassland data from $0.25^\circ \times 0.25^\circ$ resolution to the 250 m × 250
 266 m resolution of the erosion model is performed through a probabilistic land use allocation scheme
 267 based on classification rules applied to auxiliary information (i.e., a crop suitability index, more detail
 268 in Borrelli et al.⁴⁰). Finally, the C-factor of the cropland is defined at sub-national administrative level
 269 (Global Administrative Unit Levels) based on the Food and Agriculture Organization's (FAO)
 270 FAOSTAT database, which allowed to statistically describe typical crop rotations in each region. The
 271 C-factor of the croplands ranges from 0.131 (Northern Suriname) to 0.332 (Northeast Brazil).
 272

273 Following the assumption of Lugato et al.⁴⁴ for eroded carbon, we assume that 30% of the eroded soil
 274 flux is not redeposited on land and enters riverine systems. The fraction of eroded Hg which enters
 275 aquatic systems is uncertain, depending on hillslopes dynamics and flow patterns that are not
 276 explicitly modeled by the RUSLE-based framework, as well as whether Hg would be selectively
 277 eroded relative to carbon. We recognize that this assumption introduces uncertainty into our
 278 calculations, and assume that the fraction of eroded soil which enters riverine systems can vary
 279 between 5–47%, the range reported by Van Oost et al.⁴⁵ We calculate the eroded flux of Hg from land
 280 by multiplying the soil flux by the median Hg concentration in Amazon forested soils from a literature
 281 review (86 ng g⁻¹; see SI Spreadsheet).
 282

283 For each Amazon scenario, we tabulate the Hg erosion fluxes in Table S6. Erosion in the HIST
 284 scenario represents a flux of 64 Mg yr⁻¹ (uncertainty range: 11–100 Mg yr⁻¹). Erosion is enhanced in
 285 the deforestation scenarios, ranging from +14% increase in GOV to a 96% increase in the extreme
 286 SAV scenario. The absolute magnitudes of erosion flux changes are smaller than the perturbations in
 287 the land-air flux, driven by changes in Hg⁰ soil emissions and dry deposition (Table S6). Overall,
 288 perturbations to the erosion flux are approximately 14% of the perturbations to the land-air flux due to
 289 deforestation. A previous field study⁵ has also suggested that the majority of flux changes after
 290 deforestation occurs through atmospheric exchange (97%) rather than erosion to riverine systems.
 291 Therefore, the land-air changes to the fluxes play the larger role in the impact of deforestation on the
 292 mass balance of Hg in soils. Nevertheless, changes to erosion will affect downstream Hg
 293 concentrations and the methylation potential after deforestation^{5,29}, which would be important to
 294 consider when assessing the impact of deforestation on local ecosystems.
 295

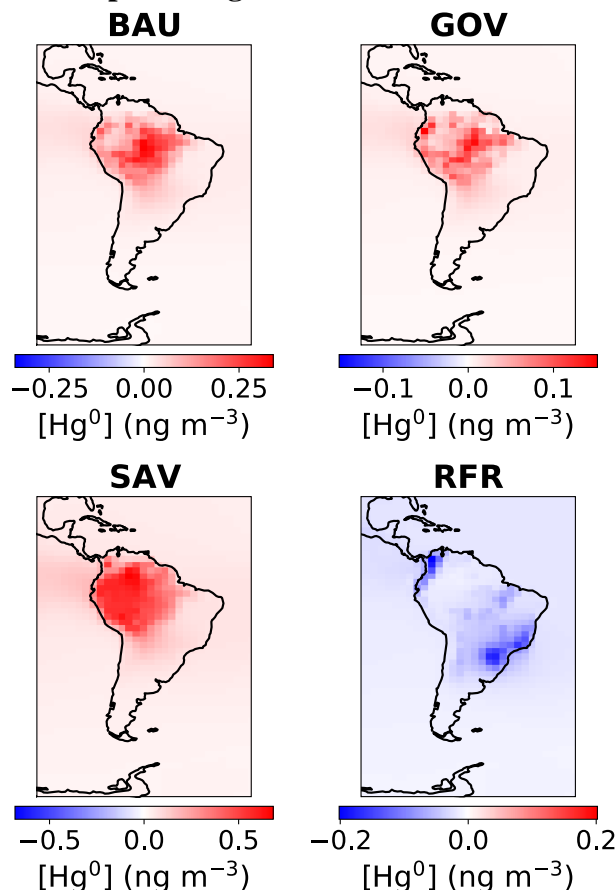
296 **Table S6.** Soil erosion fluxes for the Amazon basin calculated by the erosion model GloSEM. The
 297 simulations names refer to the following scenarios: reference (HIST), Business-as-usual (BAU),
 298 Governance (GOV), and Savannization (SAV).

Scenario	HIST	BAU	GOV	SAV
Soil loss (Mt yr ⁻¹)	2467	3276	2816	4834
30% of soil loss (Mt yr ⁻¹) ^a	740	983	845	1450
[5%–47%]	[123–1159]	[164–1540]	[141–1323]	[242–2272]
Hg erosion (Mg yr ⁻¹)	64	85	73	125
[uncertainty range]	[11–100]	[14–132]	[12–114]	[21–195]
Change from HIST (Mg yr ⁻¹)	-	21	9	61
(relative change)		(+33%)	(+14%)	(+96%)
Land-air flux change from HIST (Mg yr ⁻¹)	-	153	61	441

299 ^a This is the flux assumed to be entering riverine systems

300
301

302 **Section S7. Impacts on atmospheric Hg concentrations**



303
 304 **Figure S11.** Annual mean differences in simulated atmospheric Hg^0 concentration at the surface
 305 between scenarios — Business-as-usual (BAU), Governance (GOV), Savannization (SAV), and global
 306 reforestation (RFR) — and the HIST reference simulation.

307
 308 **Supplementary References**

- 309 (1) Khan, T. R.; Obrist, D.; Agnan, Y.; Selin, N. E.; Perlinger, J. A. Atmosphere-Terrestrial Exchange
 310 of Gaseous Elemental Mercury: Parameterization Improvement through Direct Comparison with
 311 Measured Ecosystem Fluxes. *Environ. Sci.: Processes Impacts* **2019**, *21* (10), 1699–1712.
 312 <https://doi.org/10.1039/C9EM00341J>.
- 313 (2) Selin, N. E.; Jacob, D. J.; Yantosca, R. M.; Strode, S.; Jaeglé, L.; Sunderland, E. M. Global 3-D
 314 Land-Ocean-Atmosphere Model for Mercury: Present-Day versus Preindustrial Cycles and
 315 Anthropogenic Enrichment Factors for Deposition. *Global Biogeochem. Cycles* **2008**, *22* (2),
 316 GB2011. <https://doi.org/10.1029/2007GB003040>.
- 317 (3) Verstraete, M. M. Radiation Transfer in Plant Canopies: Transmission of Direct Solar Radiation
 318 and the Role of Leaf Orientation. *J. Geophys. Res.* **1987**, *92* (D9), 10985.
 319 <https://doi.org/10.1029/JD092iD09p10985>.
- 320 (4) Zhou, J.; Wang, Z.; Zhang, X.; Driscoll, C. T.; Lin, C.-J. Soil–Atmosphere Exchange Flux of
 321 Total Gaseous Mercury (TGM) at Subtropical and Temperate Forest Catchments. *Atmos. Chem.*
 322 *Phys.* **2020**, *20* (24), 16117–16133. <https://doi.org/10.5194/acp-20-16117-2020>.
- 323 (5) Eckley, C. S.; Eagles-Smith, C.; Tate, M. T.; Krabbenhoft, D. P. Surface–Air Mercury Fluxes and
 324 a Watershed Mass Balance in Forested and Harvested Catchments. *Environmental Pollution*
 325 **2021**, *277*, 116869. <https://doi.org/10.1016/j.envpol.2021.116869>.
- 326 (6) Zhu, W.; Lin, C.-J.; Wang, X.; Sommar, J.; Fu, X.; Feng, X. Global Observations and Modeling
 327 of Atmosphere–Surface Exchange of Elemental Mercury: A Critical Review. *Atmos. Chem.*
 328 *Phys.* **2016**, *16* (7), 4451–4480. <https://doi.org/10.5194/acp-16-4451-2016>.

- 329 (7) Agnan, Y.; Le Dantec, T.; Moore, C. W.; Edwards, G. C.; Obrist, D. New Constraints on
 330 Terrestrial Surface–Atmosphere Fluxes of Gaseous Elemental Mercury Using a Global
 331 Database. *Environ. Sci. Technol.* **2016**, *50* (2), 507–524. <https://doi.org/10.1021/acs.est.5b04013>.
- 332 (8) Magarelli, G.; Fostier, A. Influence of Deforestation on the Mercury Air/Soil Exchange in the
 333 Negro River Basin, Amazon. *Atmos. Environ.* **2005**, *39* (39), 7518–7528.
 334 <https://doi.org/10.1016/j.atmosenv.2005.07.067>.
- 335 (9) Almeida, M. D.; Marins, R. V.; Paraquetti, H. H. M.; Bastos, W. R.; Lacerda, L. D. Mercury
 336 Degassing from Forested and Open Field Soils in Rondônia, Western Amazon, Brazil.
 337 *Chemosphere* **2009**, *77* (1), 60–66. <https://doi.org/10.1016/j.chemosphere.2009.05.018>.
- 338 (10) Carpi, A.; Fostier, A. H.; Orta, O. R.; dos Santos, J. C.; Gittings, M. Gaseous Mercury Emissions
 339 from Soil Following Forest Loss and Land Use Changes: Field Experiments in the United States
 340 and Brazil. *Atmos. Environ.* **2014**, *96*, 423–429. <https://doi.org/10.1016/j.atmosenv.2014.08.004>.
- 341 (11) Song, S.; Selin, N. E.; Soerensen, A. L.; Angot, H.; Artz, R.; Brooks, S.; Brunke, E.-G.; Conley,
 342 G.; Dommergue, A.; Ebinghaus, R.; Holsen, T. M.; Jaffe, D. A.; Kang, S.; Kelley, P.; Luke, W.
 343 T.; Magand, O.; Marumoto, K.; Pfaffhuber, K. A.; Ren, X.; Sheu, G.-R.; Slemr, F.; Warneke, T.;
 344 Weigelt, A.; Weiss-Penzias, P.; Wip, D. C.; Zhang, Q. Top-down Constraints on Atmospheric
 345 Mercury Emissions and Implications for Global Biogeochemical Cycling. *Atmos. Chem. Phys.*
 346 **2015**, *15* (12), 7103–7125. <https://doi.org/10.5194/acp-15-7103-2015>.
- 347 (12) Horowitz, H. M.; Jacob, D. J.; Zhang, Y.; Dibble, T. S.; Slemr, F.; Amos, H. M.; Schmidt, J. A.;
 348 Corbitt, E. S.; Marais, E. A.; Sunderland, E. M. A New Mechanism for Atmospheric Mercury
 349 Redox Chemistry: Implications for the Global Mercury Budget. *Atmos. Chem. Phys.* **2017**, *17*
 350 (10), 6353–6371. <https://doi.org/10.5194/acp-17-6353-2017>.
- 351 (13) Gamby, R. L.; Hammerschmidt, C. R.; Costello, D. M.; Lamborg, C. H.; Runkle, J. R.
 352 Deforestation and Cultivation Mobilize Mercury from Topsoil. *Science of The Total*
 353 *Environment* **2015**, *532*, 467–473. <https://doi.org/10.1016/j.scitotenv.2015.06.025>.
- 354 (14) Homann, P. S.; Darbyshire, R. L.; Bormann, B. T.; Morrisette, B. A. Forest Structure Affects
 355 Soil Mercury Losses in the Presence and Absence of Wildfire. *Environ. Sci. Technol.* **2015**, *49*
 356 (21), 12714–12722. <https://doi.org/10.1021/acs.est.5b03355>.
- 357 (15) Fostier, A. H.; Forti, M. C.; Guimarães, J. R.; Melfi, A. J.; Boulet, R.; Espirito Santo, C. M.;
 358 Krug, F. J. Mercury Fluxes in a Natural Forested Amazonian Catchment (Serra Do Navio,
 359 Amapá State, Brazil). *Sci. Total Environ.* **2000**, *260* (1–3), 201–211.
 360 [https://doi.org/10.1016/S0048-9697\(00\)00564-7](https://doi.org/10.1016/S0048-9697(00)00564-7).
- 361 (16) Gerson, J. R.; Szponar, N.; Zambrano, A. A.; Bergquist, B.; Broadbent, E.; Driscoll, C. T.;
 362 Erkenswick, G.; Evers, D. C.; Fernandez, L. E.; Hsu-Kim, H.; Inga, G.; Lansdale, K. N.;
 363 Marchese, M. J.; Martinez, A.; Moore, C.; Pan, W. K.; Purizaca, R. P.; Sánchez, V.; Silman, M.;
 364 Ury, E. A.; Vega, C.; Watsa, M.; Bernhardt, E. S. Amazon Forests Capture High Levels of
 365 Atmospheric Mercury Pollution from Artisanal Gold Mining. *Nat Commun* **2022**, *13* (1), 559.
 366 <https://doi.org/10.1038/s41467-022-27997-3>.
- 367 (17) Almeida, M. D.; Lacerda, L. D.; Bastos, W. R.; Herrmann, J. C. Mercury Loss from Soils
 368 Following Conversion from Forest to Pasture in Rondônia, Western Amazon, Brazil.
 369 *Environmental Pollution* **2005**, *137* (2), 179–186. <https://doi.org/10.1016/j.envpol.2005.02.026>.
- 370 (18) Lacerda, L. D.; de Souza, M.; Ribeiro, M. G. The Effects of Land Use Change on Mercury
 371 Distribution in Soils of Alta Floresta, Southern Amazon. *Environmental Pollution* **2004**, *129* (2),
 372 247–255. <https://doi.org/10.1016/j.envpol.2003.10.013>.
- 373 (19) Béliveau, A.; Lucotte, M.; Davidson, R.; do Canto Lopes, L. O.; Paquet, S. Early Hg Mobility in
 374 Cultivated Tropical Soils One Year after Slash-and-Burn of the Primary Forest, in the Brazilian
 375 Amazon. *Science of The Total Environment* **2009**, *407* (15), 4480–4489.
 376 <https://doi.org/10.1016/j.scitotenv.2009.04.012>.
- 377 (20) Béliveau, A.; Lucotte, M.; Davidson, R.; Paquet, S.; Mertens, F.; Passos, C. J.; Romana, C. A.
 378 Reduction of Soil Erosion and Mercury Losses in Agroforestry Systems Compared to Forests
 379 and Cultivated Fields in the Brazilian Amazon. *Journal of Environmental Management* **2017**,
 380 *203*, 522–532. <https://doi.org/10.1016/j.jenvman.2017.07.037>.
- 381 (21) Patry, C.; Davidson, R.; Lucotte, M.; Béliveau, A. Impact of Forested Fallows on Fertility and
 382 Mercury Content in Soils of the Tapajós River Region, Brazilian Amazon. *Science of The Total*
 383 *Environment* **2013**, *458–460*, 228–237. <https://doi.org/10.1016/j.scitotenv.2013.04.037>.

- 384 (22)Comte, I.; Lucotte, M.; Davidson, R.; Reis de Carvalho, C. J.; de Assis Oliveira, F.; Rousseau, G.
 385 X. Impacts of Land Uses on Mercury Retention in Long-Time Cultivated Soils, Brazilian
 386 Amazon. *Water Air Soil Pollut* **2013**, 224 (4), 1515. <https://doi.org/10.1007/s11270-013-1515-3>.
 387 (23)Mainville, N.; Webb, J.; Lucotte, M.; Davidson, R.; Betancourt, O.; Cueva, E.; Mergler, D.
 388 Decrease of Soil Fertility and Release of Mercury Following Deforestation in the Andean
 389 Amazon, Napo River Valley, Ecuador. *Science of The Total Environment* **2006**, 368 (1), 88–98.
 390 <https://doi.org/10.1016/j.scitotenv.2005.09.064>.
 391 (24)Roulet, M.; Lucotte, M.; Saint-Aubin, A.; Tran, S.; Rhéault, I.; Farella, N.; De Jesus Da Silva, E.;
 392 Dezencourt, J.; Sousa Passos, C.-J.; Santos Soares, G.; Guimarães, J.-R. D.; Mergler, D.;
 393 Amorim, M. The Geochemistry of Mercury in Central Amazonian Soils Developed on the Alter-
 394 Do-Chão Formation of the Lower Tapajós River Valley, Pará State, Brazil. *Science of The Total*
 395 *Environment* **1998**, 223 (1), 1–24. [https://doi.org/10.1016/S0048-9697\(98\)00265-4](https://doi.org/10.1016/S0048-9697(98)00265-4).
 396 (25)Wasserman, J. C.; Campos, R. C.; Hacon, S. de S.; Farias, R. A.; Caires, S. M. Mercury in Soils
 397 and Sediments from Gold Mining Liabilities in Southern Amazonia. *Quím. Nova* **2007**, 30 (4).
 398 <https://doi.org/10.1590/S0100-40422007000400003>.
 399 (26)Wang, X.; Lin, C.-J.; Yuan, W.; Sommar, J.; Zhu, W.; Feng, X. Emission-Dominated Gas
 400 Exchange of Elemental Mercury Vapor over Natural Surfaces in China. *Atmos. Chem. Phys.*
 401 **2016**, 16 (17), 11125–11143. <https://doi.org/10.5194/acp-16-11125-2016>.
 402 (27)Mazur, M.; Mitchell, C. P. J.; Eckley, C. S.; Eggert, S. L.; Kolka, R. K.; Sebestyen, S. D.; Swain,
 403 E. B. Gaseous Mercury Fluxes from Forest Soils in Response to Forest Harvesting Intensity: A
 404 Field Manipulation Experiment. *Science of The Total Environment* **2014**, 496, 678–687.
 405 <https://doi.org/10.1016/j.scitotenv.2014.06.058>.
 406 (28)Ma, M.; Wang, D.; Sun, R.; Shen, Y.; Huang, L. Gaseous Mercury Emissions from Subtropical
 407 Forested and Open Field Soils in a National Nature Reserve, Southwest China. *Atmospheric*
 408 *Environment* **2013**, 64, 116–123. <https://doi.org/10.1016/j.atmosenv.2012.09.038>.
 409 (29)Eklöf, K.; Lidskog, R.; Bishop, K. Managing Swedish Forestry’s Impact on Mercury in Fish:
 410 Defining the Impact and Mitigation Measures. *Ambio* **2016**, 45 (S2), 163–174.
 411 <https://doi.org/10.1007/s13280-015-0752-7>.
 412 (30)De Wit, H. A.; Granhus, A.; Lindholm, M.; Kainz, M. J.; Lin, Y.; Braaten, H. F. V.; Blaszcak, J.
 413 Forest Harvest Effects on Mercury in Streams and Biota in Norwegian Boreal Catchments.
 414 *Forest Ecology and Management* **2014**, 324, 52–63.
 415 <https://doi.org/10.1016/j.foreco.2014.03.044>.
 416 (31)Abraham, J.; Dowling, K.; Florentine, S. Effects of Prescribed Fire and Post-Fire Rainfall on
 417 Mercury Mobilization and Subsequent Contamination Assessment in a Legacy Mine Site in
 418 Victoria, Australia. *Chemosphere* **2018**, 190, 144–153.
 419 <https://doi.org/10.1016/j.chemosphere.2017.09.117>.
 420 (32)Howard, D.; Macsween, K.; Edwards, G. C.; Desservettaz, M.; Guérette, E.-A.; Paton-Walsh, C.;
 421 Surawski, N. C.; Sullivan, A. L.; Weston, C.; Volkova, L.; Powell, J.; Keywood, M. D.; Reisen,
 422 F.; (Mick) Meyer, C. P. Investigation of Mercury Emissions from Burning of Australian
 423 Eucalypt Forest Surface Fuels Using a Combustion Wind Tunnel and Field Observations.
 424 *Atmospheric Environment* **2019**, 202, 17–27. <https://doi.org/10.1016/j.atmosenv.2018.12.015>.
 425 (33)Feinberg, A.; Dlamini, T.; Jiskra, M.; Shah, V.; Selin, N. E. Evaluating Atmospheric Mercury
 426 (Hg) Uptake by Vegetation in a Chemistry-Transport Model. *Environ. Sci.: Processes Impacts*
 427 **2022**, 24 (9), 1303–1318. <https://doi.org/10.1039/D2EM00032F>.
 428 (34)Hurt, G. C.; Chini, L.; Sahajpal, R.; Frolking, S.; Bodirsky, B. L.; Calvin, K.; Doelman, J. C.;
 429 Fisk, J.; Fujimori, S.; Klein Goldewijk, K.; Hasegawa, T.; Havlik, P.; Heinemann, A.;
 430 Humpenöder, F.; Jungclaus, J.; Kaplan, J. O.; Kennedy, J.; Krisztin, T.; Lawrence, D.;
 431 Lawrence, P.; Ma, L.; Mertz, O.; Pongratz, J.; Popp, A.; Poulter, B.; Riahi, K.; Shevliakova, E.;
 432 Stehfest, E.; Thornton, P.; Tubiello, F. N.; van Vuuren, D. P.; Zhang, X. Harmonization of
 433 Global Land Use Change and Management for the Period 850–2100 (LUH2) for CMIP6. *Geosci.*
 434 *Model Dev.* **2020**, 13 (11), 5425–5464. <https://doi.org/10.5194/gmd-13-5425-2020>.
 435 (35)Michelazzo, P. A. M.; Fostier, A. H.; Magarelli, G.; Santos, J. C.; de Carvalho, J. A. Mercury
 436 Emissions from Forest Burning in Southern Amazon. *Geophys. Res. Lett.* **2010**, 37 (9), L09809.
 437 <https://doi.org/10.1029/2009GL042220>.

- 438 (36)Melendez-Perez, J. J.; Fostier, A. H.; Carvalho, J. A.; Windmöller, C. C.; Santos, J. C.; Carpi, A.
439 Soil and Biomass Mercury Emissions during a Prescribed Fire in the Amazonian Rain Forest.
440 *Atmospheric Environment* **2014**, *96*, 415–422. <https://doi.org/10.1016/j.atmosenv.2014.06.032>.
- 441 (37)Soares-Filho, B. S.; Nepstad, D. C.; Curran, L. M.; Cerqueira, G. C.; Garcia, R. A.; Ramos, C. A.;
442 Voll, E.; McDonald, A.; Lefebvre, P.; Schlesinger, P. Modelling Conservation in the Amazon
443 Basin. *Nature* **2006**, *440* (7083), 520–523. <https://doi.org/10.1038/nature04389>.
- 444 (38)Roulet, M.; Lucotte, M.; Farella, N.; Serique, G.; Coelho, H.; Passos, S.; Mergler, D. Effects of
445 Recent Human Colonization on the Presence of Mercury in Amazonian Ecosystems. *Water Air*
446 *Soil Pollut.* **1999**, *112*, 297–313.
- 447 (39)Renard, K. G.; Foster, G. R.; Weesies, G. A.; McCool, D. K.; Yoder, D. C. Predicting Soil
448 Erosion by Water: A Guide to Conservation Planning with the Revised Universal Soil Loss
449 Equation (RUSLE). *Agriculture handbook* **1997**, *703*.
- 450 (40)Borrelli, P.; Robinson, D. A.; Panagos, P.; Lugato, E.; Yang, J. E.; Alewell, C.; Wuepper, D.;
451 Montanarella, L.; Ballabio, C. Land Use and Climate Change Impacts on Global Soil Erosion by
452 Water (2015-2070). *Proc. Natl. Acad. Sci. U.S.A.* **2020**, *117* (36), 21994–22001.
453 <https://doi.org/10.1073/pnas.2001403117>.
- 454 (41)Borrelli, P.; Robinson, D. A.; Fleischer, L. R.; Lugato, E.; Ballabio, C.; Alewell, C.; Meusburger,
455 K.; Modugno, S.; Schütt, B.; Ferro, V.; Bagarello, V.; Oost, K. V.; Montanarella, L.; Panagos, P.
456 An Assessment of the Global Impact of 21st Century Land Use Change on Soil Erosion. *Nat*
457 *Commun* **2017**, *8* (1), 2013. <https://doi.org/10.1038/s41467-017-02142-7>.
- 458 (42)Panagos, P.; Borrelli, P.; Meusburger, K.; Yu, B.; Klik, A.; Jae Lim, K.; Yang, J. E.; Ni, J.; Miao,
459 C.; Chattopadhyay, N.; Sadeghi, S. H.; Hazbavi, Z.; Zabihi, M.; Larionov, G. A.; Krasnov, S. F.;
460 Gorobets, A. V.; Levi, Y.; Erpul, G.; Birkel, C.; Hoyos, N.; Naipal, V.; Oliveira, P. T. S.;
461 Bonilla, C. A.; Meddi, M.; Nel, W.; Al Dashti, H.; Boni, M.; Diodato, N.; Van Oost, K.;
462 Nearing, M.; Ballabio, C. Global Rainfall Erosivity Assessment Based on High-Temporal
463 Resolution Rainfall Records. *Sci Rep* **2017**, *7* (1), 4175. [https://doi.org/10.1038/s41598-017-](https://doi.org/10.1038/s41598-017-04282-8)
464 [04282-8](https://doi.org/10.1038/s41598-017-04282-8).
- 465 (43)Hengl, T.; De Jesus, J. M.; MacMillan, R. A.; Batjes, N. H.; Heuvelink, G. B. M.; Ribeiro, E.;
466 Samuel-Rosa, A.; Kempen, B.; Leenaars, J. G. B.; Walsh, M. G.; Gonzalez, M. R. SoilGrids1km
467 — Global Soil Information Based on Automated Mapping. *PLoS ONE* **2014**, *9* (8), e105992.
468 <https://doi.org/10.1371/journal.pone.0105992>.
- 469 (44)Lugato, E.; Smith, P.; Borrelli, P.; Panagos, P.; Ballabio, C.; Orgiazzi, A.; Fernandez-Ugalde, O.;
470 Montanarella, L.; Jones, A. Soil Erosion Is Unlikely to Drive a Future Carbon Sink in Europe.
471 *Sci. Adv.* **2018**, *4* (11), eaau3523. <https://doi.org/10.1126/sciadv.aau3523>.
- 472 (45)Van Oost, K.; Quine, T. A.; Govers, G.; De Gryze, S.; Six, J.; Harden, J. W.; Ritchie, J. C.;
473 McCarty, G. W.; Heckrath, G.; Kosmas, C.; Giraldez, J. V.; Da Silva, J. R. M.; Merckx, R. The
474 Impact of Agricultural Soil Erosion on the Global Carbon Cycle. *Science* **2007**, *318* (5850), 626–
475 629. <https://doi.org/10.1126/science.1145724>.
- 476